Journal of Renewable and Sustainable Energy ARTICLE scitation.org/journal/rse

Large-eddy simulation of helical- and straight-bladed vertical-axis wind turbines in boundary layer turbulence

Cite as: J. Renewable Sustainable Energy **14**, 053301 (2022); doi: 10.1063/5.0100169
Submitted: 21 May 2022 · Accepted: 1 August 2022 ·
Published Online: 1 September 2022

Masoumeh Gharaati,[1] Shuolin Xiao,[1,a)] Nathaniel J. Wei,[2] Luis A. Martínez-Tossas,[3] John O. Dabiri,[2,4] and Di Yang[1,b)]

AFFILIATIONS

[1]Department of Mechanical Engineering, University of Houston, Houston, Texas 77204, USA
[2]Graduate Aeronautical Laboratories, California Institute of Technology, Pasadena, California 91125, USA
[3]National Renewable Energy Laboratory, Golden, Colorado 80401, USA
[4]Department of Mechanical and Civil Engineering, California Institute of Technology, Pasadena, California 91125, USA

[a)]**Current address:** School of Civil and Environmental Engineering, Cornell University, Ithaca, New York 14853, USA.
[b)]**Author to whom correspondence should be addressed:** diyang@uh.edu

ABSTRACT

Turbulent wake flows behind helical- and straight-bladed vertical axis wind turbines (VAWTs) in boundary layer turbulence are numerically studied using the large-eddy simulation (LES) method combined with the actuator line model. Based on the LES data, systematic statistical analyses are performed to explore the effects of blade geometry on the characteristics of the turbine wake. The time-averaged velocity fields show that the helical-bladed VAWT generates a mean vertical velocity along the center of the turbine wake, which causes a vertical inclination of the turbine wake and alters the vertical gradient of the mean streamwise velocity. Consequently, the intensities of the turbulent fluctuations and Reynolds shear stresses are also affected by the helical-shaped blades when compared with those in the straight-bladed VAWT case. The LES results also show that reversing the twist direction of the helical-bladed VAWT causes the spatial patterns of the turbulent wake flow statistics to be reversed in the vertical direction. Moreover, the mass and kinetic energy transports in the turbine wakes are directly visualized using the transport tube method, and the comparison between the helical- and straight-bladed VAWT cases show significant differences in the downstream evolution of the transport tubes.

I. INTRODUCTION

Vertical-axis wind turbines (VAWTs) and horizontal-axis wind turbines (HAWTs) are the two main types of wind-energy extraction devices.[1,2] HAWTs have proven themselves to be an effective energy-harvesting technology over the past several decades and are widely used in most commercial wind farms today in both onshore and offshore contexts.[2–5] Modern commercial HAWTs can produce megawatts of power with high power-conversion efficiencies.[2,6] Despite their commercial success, the large size of HAWTs (whose rotor diameters are often in excess of 100 m) creates some logistical difficulties. Aerodynamically, the optimal spacing in the streamwise direction of HAWTs in a wind farm may be as much as 15 turbine rotor diameters or larger,[7] which translates to large amounts of land or offshore water area required for effective operation and correspondingly lower wind-farm power densities. The size of HAWT blades and towers also creates logistical difficulties for construction, transport, and maintenance.[8] Additionally, HAWTs must face the incoming wind for optimal power production, necessitating complex yaw-control schemes to compensate for changing wind direction.[9]

VAWTs, on the other hand, have wakes that recover relatively quickly, in some cases within six turbine diameters downstream.[10] They can thus be placed in closely packed arrays for improved wind-farm power densities. Furthermore, VAWTs placed in close proximity to each other can mutually benefit from aerodynamic interactions for improved overall efficiencies.[11,12] The performance of a VAWT is insensitive to wind direction, eliminating the need for yaw-control systems. VAWTs also typically have smaller diameters and their electrical components may be mounted closer to the ground for ease of

operations and maintenance. Finally, VAWTs tend to operate at lower tip-speed ratios (TSRs) than HAWTs and thus may generate less noise.[13,14] For these reasons, VAWTs represent a potential wind-energy solution for contexts in which traditional HAWT farms are impractical or infeasible, such as sites with limited land area or frequently changing wind direction.

Unlike HAWTs, whose designs are relatively uniform, there exist several different types of VAWT designs that are distinguished by their blade geometries, including Savonius turbines, Darrieus turbines with curved blades, straight-bladed Darrieus turbines, and helical-bladed Darrieus turbines.[13] Among these different types, the straight-bladed VAWTs have been studied and deployed more frequently due to their relatively simple blade geometry.[12,14–22] A number of laboratory experiments have been conducted to gain fundamental understanding of the VAWT wake flows under uniform mean inflow conditions.[12,15–17,19,20,23] Several field experiments have also been performed to study the interactions of straight-bladed VAWTs with turbulent wind in the atmospheric boundary layer (ABL), which have provided crucial information for assessing the performance of VAWTs in realistic environments.[10,11,18,22]

In recent years, helical-bladed VAWTs have begun to attract more attention due to several potential advantages, such as a low cut-in wind speed, low temporal oscillations in torque and power, and low noise level.[24–27] Several numerical studies have used the unsteady Reynolds averaged Navier–Stokes (URANS) modeling approach to study the aerodynamic performance and power production of helical-bladed VAWTs in comparison with straight-bladed VAWTs.[25–28] Wei *et al.*[22] performed field experiments using three-dimensional particle-tracking velocimetry to measure the time-averaged velocities and vorticities downstream of a full-scale helical-bladed VAWT and compared its near-wake flow structures with those downstream of a straight-bladed VAWT. Despite these recent advances, our current understanding of the wake characteristics of helical-bladed VAWTs is still limited with respect to straight-bladed VAWTs. For potential applications in large-scale commercial VAWT farms, it is crucial to understand the characteristics of the wake flows behind helical-bladed VAWTs, such as the mean wind-speed recovery, turbulence intensity, and mass and energy exchanges between the low-speed wake flow and the high-speed surrounding flow, which are important for assessing the impact of upstream turbines on the performance of downstream turbines in large turbine arrays.[6,21,29–34]

In recent years, large-eddy simulation (LES) has become a promising tool for modeling the turbulent flow dynamics in the turbine wake flows and in the turbine array boundary layers (i.e., in large wind farms).[30,35–38] In particular, LES equipped with the actuator line model (ALM) for wind turbines has shown successful applications in modeling HAWTs and VAWTs wake flows.[14,37–48] Several recent LES studies on straight-bladed VAWTs have provided valuable insight for understanding the characteristics of the turbine wake flows under various laboratory and ABL flow conditions. In this study, we adopt the Johns Hopkins University LES model, LESGO, as the main wind turbulence solver.[49] LESGO is equipped with an ALM module implemented originally for modeling HAWTs.[37,41,42,50] This existing ALM module is modified in the present study to model the straight- and helical-bladed VAWTs.

The present work aims to study the effects of blade geometry on the wake flow characteristics of VAWTs. To this end, three VAWTs with different blade geometries are considered: one straight-bladed VAWT and two helical-bladed VAWTs with opposite blade twist directions but the same twist rate of $39.69^\circ/\mathrm{m}$ along the vertical direction. The straight-bladed VAWT can be regarded as a special version of the helical-bladed VAWT with zero blade twist angle. These three VAWTs have identical parameters, including the rotor equator height (8.2 m), rotor diameter (1.8 m), blade vertical length (3.2 m), and blade cross-sectional geometry. A concurrent precursor simulation method is used to generate realistic boundary layer turbulence inflow condition with a mean wind speed of 11.79 m/s at the VAWT equator height. Based on statistically identical inflow conditions, the interactions of the three different VAWTs with the boundary layer turbulence are simulated using the LES model. The TSR for VAWT rotation is kept the same at 1.19 for all three VAWT cases to allow direct comparison of the simulation results. The key VAWT parameters, wind speed, and TSR value are chosen to match the field experiments of Wei *et al.*[22] Based on the LES data, the effects of the helical-shaped blades on the characteristics of the turbulent wake flows are systematically investigated by direct observations of the instantaneous velocities, comparison of the time-averaged velocities, as well as analysis of the statistics of the turbulent velocity fluctuations in the turbine wake region.

The remainder of this paper is organized as follows. The LES model for wind turbulence and the actuator line model for the VAWT are introduced in Sec. II. In Sec. III, two test cases based on straight-bladed VAWTs are provided to validate the current LES model. In Sec. IV, the LES cases for studying the effects of helical-bladed VAWTs on the wake flow characteristics are presented in detail, including the case configurations, the instantaneous flow fields, and the time-averaged mean-flow and turbulent-fluctuation statistics. Finally, the implications of these results are discussed in Sec. V.

II. NUMERICAL METHOD FOR WIND TURBULENCE AND TURBINE MODEL

A. Large-eddy simulation of wind turbulence

In this study, we perform simulations of helical- and straight-bladed VAWTs interacting with fully developed wind turbulence in a neutral boundary layer. We adopt the large-eddy simulation model LESGO developed by the Turbulence Research Group at Johns Hopkins University as the main wind turbulence solver.[49] The wind turbulent flow motions are governed by the three-dimensional incompressible filtered Navier–Stokes equations

$$\nabla \cdot \tilde{\mathbf{u}} = 0, \tag{1}$$

$$\frac{\partial \tilde{\mathbf{u}}}{\partial t} + \nabla \cdot (\tilde{\mathbf{u}}\,\tilde{\mathbf{u}}) = -\frac{1}{\rho}\nabla \tilde{p} + \nu \nabla^2 \tilde{\mathbf{u}} - \nabla \cdot \boldsymbol{\tau} + \frac{\mathbf{f}_x}{\rho} - \frac{\tilde{\mathbf{f}}_\varepsilon}{\rho}. \tag{2}$$

Here, the tilde denotes filtering at the LES grid scale Δ; $\tilde{\mathbf{u}} = (\tilde{u}, \tilde{v}, \tilde{w})$ is the resolved flow velocity vector, where $\tilde{u}$, $\tilde{v}$, and $\tilde{w}$ are the corresponding components in the streamwise (x), spanwise (y), and vertical (z) directions, respectively; ν is the kinematic viscosity of air; ρ is the air density; $\tilde{p}$ is the resolved pressure; $\boldsymbol{\tau} = \widetilde{\mathbf{u}\mathbf{u}} - \tilde{\mathbf{u}}\,\tilde{\mathbf{u}}$ is the subgrid-scale (SGS) stress tensor; $\mathbf{f}_x$ is an imposed streamwise body force to drive the wind turbulence; and $\tilde{\mathbf{f}}_\varepsilon$ is a distributed body force for modeling the effect of the wind turbine on the flow. More details about $\mathbf{f}_x$ and $\tilde{\mathbf{f}}_\varepsilon$ are given below.

To close Eq. (2), the deviatoric part of the SGS stress tensor $\boldsymbol{\tau}^d$ is parameterized using the eddy-viscosity type model,[51,52]

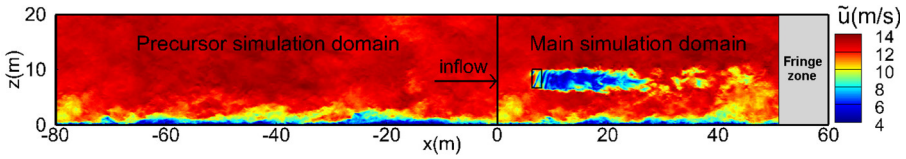

FIG. 1. Illustration of concurrent precursor method for modeling VAWT in the boundary layer turbulence.

$\boldsymbol{\tau}^d = -2\nu_\tau \tilde{\mathbf{S}} = -2(c_s\Delta)^2|\tilde{\mathbf{S}}|\tilde{\mathbf{S}}$, where ν_τ is the SGS eddy viscosity, c_s is the Smagorinsky coefficient, $\tilde{\mathbf{S}} = [\nabla\tilde{\mathbf{u}} + (\nabla\tilde{\mathbf{u}})^T]/2$ is the resolved strain rate tensor, and $|\tilde{\mathbf{S}}| \equiv \sqrt{2\tilde{\mathbf{S}} : (\tilde{\mathbf{S}})^T}$ is the magnitude of $\tilde{\mathbf{S}}$. The trace of the SGS stress tensor $\mathrm{tr}(\boldsymbol{\tau})$ is not modeled explicitly, but instead is absorbed into the pressure term as commonly done in the LES of incompressible turbulence.[52–55] In LESGO, the instantaneous local value of c_s is calculated dynamically during the simulation using the Lagrangian-averaged scale-dependent dynamic (LASD) SGS model.[56] The LES utilizing the LASD model has been used in a number of prior studies on wind-turbine wake flows.[30,35,36,57–59]

A concurrent precursor method is used to provide the fully developed neutral boundary layer turbulence inflow condition for modeling the wind–VAWT interaction.[60] As shown in Fig. 1, the overall simulation domain consists of two sub-domains that are computed simultaneously in the LES, i.e., the precursor simulation domain for the fully developed boundary layer turbulence without VAWTs and the main simulation domain for turbulence interacting with VAWTs. The precursor simulation uses periodic boundary conditions in the x- and y-directions, and the mean flow is driven by a constant pressure gradient imposed in the x-direction,[30,36,60]

$$\mathbf{f}_x = -\frac{\mathrm{d}p_\infty}{\mathrm{d}x}\hat{\mathbf{e}}_x, \tag{3}$$

where $\hat{\mathbf{e}}_x$ is the unit vector in the x-direction. The turbine-induced force is set to $\tilde{\mathbf{f}}_\varepsilon = 0$ in the precursor domain. Different from the precursor simulation, the main simulation with the VAWTs uses the inflow–outflow conditions in the x-direction and the periodic condition in the y-direction. The fully developed boundary layer inflow condition extracted from the precursor simulation domain is fed into the upstream end of the main simulation domain to push the wind turbulence through the simulation domain toward the outflow boundary at the downstream end of the main simulation domain. Associated with these inflow–outflow streamwise boundary conditions, the streamwise body force $\mathbf{f}_x$ is set to be zero in the main simulation domain. The turbine-induced force $\tilde{\mathbf{f}}_\varepsilon$ is modeled using the actuator line model, which is discussed in Sec. II B.

The LESGO model uses the Fourier-series-based pseudo-spectral method for the spatial discretizations in the x- and y-directions. In order to use the inflow–outflow condition properly in a pseudo-spectral flow solver, the fringe-zone method is used for the main simulation.[61,62] As shown in Fig. 1, a fringe zone of finite streamwise length L_{fr} adjacent to the outflow boundary is used to achieve a smooth transition of the simulated wind turbulence in the far wake of the turbines back to its imposed value at the inflow boundary, which allows the simulation of the non-periodic turbine wake flows using the periodic pseudo-spectral flow solver. Specifically, in the fringe zone, $x_{fr} \le x \le L_x$, the flow velocity vector is imposed as

$$\tilde{\mathbf{u}}(x,y,z) = \tilde{\mathbf{u}}(x_{fr},y,z)[1-\psi(x)] + \tilde{\mathbf{u}}_{in}(y,z)\psi(x), \tag{4}$$

where L_x is the streamwise length of the main simulation domain, $x_{fr} = L_x - L_{fr}$ is the streamwise location where the fringe zone starts, $\psi(x) = 0.5 - 0.5\cos[\pi(x - x_{fr})/L_{fr}]$ is the fringe function, and $\tilde{\mathbf{u}}_{in}(y,z)$ is the inflow velocity for the main simulation provided by the precursor simulation (i.e., extracted at the downstream end of the precursor simulation domain as shown in Fig. 1). As illustrated in Fig. 2, this concurrent precursor method allows physical boundary layer turbulence inflow conditions to be obtained and used for modeling the VAWT wake flow. Details about the implementation of the concurrent precursor LES are provided in Secs. III B and IV A.

B. Actuator line model for vertical-axis wind turbines

In the current LES model, the aerodynamic forces induced by the turbine blades to the wind turbulence are computed using the ALM.[39] Let R be the radius of the VAWT rotor (i.e., the radial distance from the chord of the blade to the center axis of the VAWT), $D = 2R$ be the turbine rotor diameter, and H be the vertical height of the blade. Each VAWT blade is discretized into N_b elements, with a vertical height of $\Delta H = H/N_b$ for each blade element. For each blade element, the local relative velocity vector of the wind with respect to the element in the local (s, n) coordinate system is

$$\mathbf{V}_{\mathrm{rel}} = \mathbf{V}_{\mathrm{local}} - R\,\Omega\,\hat{\mathbf{e}}_s. \tag{5}$$

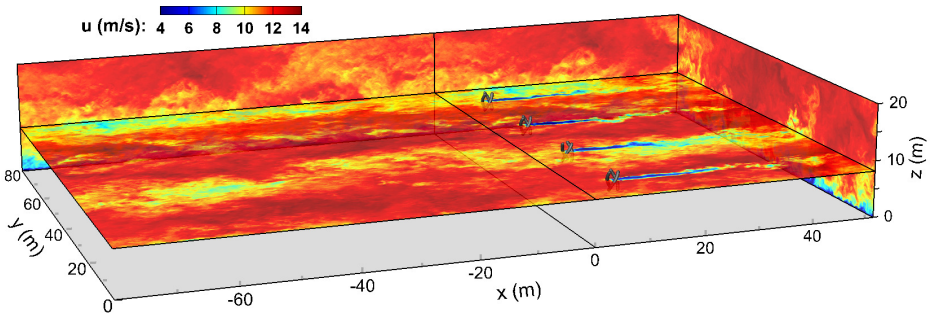

FIG. 2. Illustration of the three-dimensional flow field obtained from the current LES model. Color contours of the instantaneous streamwise velocity are shown on the domain walls and on the horizontal plane at the equator height of the VAWTs, which are shown in gray.

As illustrated in Fig. 3, s and n are the local coordinates along the tangential and radial directions of the turbine blade element, respectively; $\mathbf{V}_{\text{local}}$ is the local incoming wind velocity around the blade element projected to the (x, y)-plane through the center of the blade element; $\boldsymbol{\Omega}$ is the angular velocity of the VAWT rotation; and $\hat{\mathbf{e}}_s$ is the unit vector along the tangential direction s.

The local wind velocity vector defined in the local (s, n) coordinate system can be written as

$$\mathbf{V}_{\text{local}} = \tilde{U}_h \sin(\theta - \beta)\hat{\mathbf{e}}_s - \tilde{U}_h \cos(\theta - \beta)\hat{\mathbf{e}}_n, \tag{6}$$

where $\hat{\mathbf{e}}_n$ is the unit vector in the radial direction n, θ is the azimuthal angle for the blade rotation, $\beta = \arctan(\tilde{v}/\tilde{u})$ is the horizontal directional angle of the inflow wind velocity, and $\tilde{U}_h = \sqrt{\tilde{u}^2 + \tilde{v}^2}$ is the magnitude of the sampled horizontal velocity. In the current model, $\theta = 0$ when the blade element is located at the most upstream location (i.e., when the radial direction is aligned with the $-x$-direction), and θ increases when the blade rotates counterclockwise. Based on the direction of $\mathbf{V}_{\text{rel}}$, the local angle of attack α is calculated as

$$\alpha = \arctan\left(\frac{-\cos(\theta - \beta)}{-\sin(\theta - \beta) + R\Omega/\tilde{U}_h}\right). \tag{7}$$

For a stationary or slowly moving airfoil, the lift and drag forces can be calculated using the static lift coefficient C_L and drag coefficient C_D, respectively, based on the values of $\mathbf{V}_{\text{rel}}$ and α. However, VAWT blades rotating in turbulent wind can experience rapid changes in angle of attack, resulting in a flow phenomenon called dynamic stall.[63] In order to model the aerodynamic forces of the VAWT blades accurately, the modified Boeing–Vertol model[64] is used in the current LES model as a dynamic-stall correction. Specifically, the modified angles of attack for the lift and drag coefficients are modeled as

$$\alpha_L^* = \alpha - \gamma_L \kappa \left(\left|\frac{c\dot{\alpha}}{2V_{rel}}\right|\right)^{\frac{1}{2}} \frac{\dot{\alpha}}{|\dot{\alpha}|}, \tag{8}$$

$$\alpha_D^* = \alpha - \gamma_D \kappa \left(\left|\frac{c\dot{\alpha}}{2V_{rel}}\right|\right)^{\frac{1}{2}} \frac{\dot{\alpha}}{|\dot{\alpha}|}, \tag{9}$$

where c is the blade chord length, $\dot{\alpha} = d\alpha/dt$ is the instantaneous rate of change of α, and V_{rel} is the magnitude of the relative velocity vector $\mathbf{V}_{\text{rel}}$. The dimensionless model coefficients γ_L, γ_D, and κ are expressed as

$$\gamma_L = 1.4 - 6\left(0.06 - \frac{t_b}{c}\right), \tag{10}$$

$$\gamma_D = 1 - 2.5\left(0.06 - \frac{t_b}{c}\right), \tag{11}$$

$$\kappa = 0.75 + 0.25\frac{\dot{\alpha}}{|\dot{\alpha}|}, \tag{12}$$

where t_b is the blade thickness. Based on α_L^* and α_D^*, the lift and drag coefficients with the dynamic stall correction can be computed as[64]

$$C_L^* = \left(\frac{\alpha}{\alpha_L^* - \alpha_0}\right) C_L(\alpha_L^*), \tag{13}$$

$$C_D^* = C_D(\alpha_D^*), \tag{14}$$

where α_0 is the angle of zero lift, which is equal to 0 for symmetric airfoils. In the current LES model, the static lift coefficient C_L and drag coefficient C_D are obtained directly from the tabulated empirical data reported in Sheldahl and Klimas.[65] By projecting the lift and drag forces onto the x- and y-directions, the aerodynamics force vector acting on the kth element of a VAWT blade is $\mathbf{F}_k = F_{k,x}\hat{\mathbf{e}}_x + F_{k,y}\hat{\mathbf{e}}_y$, where $\hat{\mathbf{e}}_y$ is the unit vector in the y-direction,

$$F_{k,x} = -\frac{1}{2}\rho V_{rel}^2 c\,\Delta H\left[C_L^* \cos(\theta + \alpha) + C_D^* \sin(\theta + \alpha)\right], \tag{15}$$

$$F_{k,y} = \frac{1}{2}\rho V_{rel}^2 c\,\Delta H\left[-C_L^* \sin(\theta + \alpha) + C_D^* \cos(\theta + \alpha)\right]. \tag{16}$$

To avoid numerical instability and reduce sensitivity to the grid size when applying the aerodynamic force, $\mathbf{F}_k$ is usually distributed smoothly on the grid points around the blade element instead of at the center of the element.[14,39,44,66] In the current LES model, a three-dimensional Gaussian kernel method[39,41–43] is adopted to distribute the aerodynamic force as

$$\tilde{\mathbf{f}}_\varepsilon(x, y, z) = \sum_{k=1}^{N_b} \mathbf{F}_k G_k(x, y, z), \tag{17}$$

where

$$G_k(x, y, z) = \frac{1}{\varepsilon^3 \pi^{3/2}} \exp\left(-\frac{r_k^2}{\varepsilon^2}\right) \tag{18}$$

is the Gaussian kernel function, ε is the kernel width, and $r_k = \sqrt{(x - x_k)^2 + (y - y_k)^2 + (z - z_k)^2}$ is the distance between a space point (x, y, z) and the center point of the kth blade element

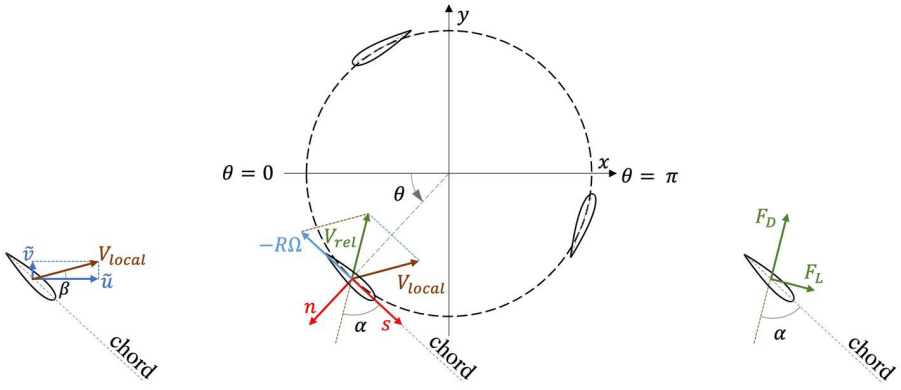

FIG. 3. Schematics of the physical quantities involved in the modeling of the VAWT blade forces.

(x_k, y_k, z_k). The distributed force $\tilde{\mathbf{f}}_\varepsilon$ calculated based on Eq. (17) is used in Eq. (2) to model the effect of turbine on the air flow.

C. Numerical methods

In the current LES model, the governing Eqs. (1) and (2) are discretized by a Fourier-series-based pseudo-spectral method on collocated grids in the x- and y-directions, and a second-order central-difference method on staggered grids in the z-direction. For the basic LES flow solver, periodic boundary conditions are used in the x- and y-directions, a local law-of-the-wall condition is applied at the bottom boundary,[53,56] and a stress-free condition is imposed at the top boundary. The momentum equation (2) is formulated and discretized in the rotational form to provide conservation of mass and kinetic energy.[67–69] The 3/2 rule is used to eliminate the aliasing error associated with the pseudo-spectral discretization of the convective terms.[70] The governing equations are integrated in time using a fractional-step method consisting of a prediction step and a correction step. In particular, in the prediction step the velocity field is advanced in time by integrating Eq. (2) using the second-order Adams–Bashforth scheme, which yields a predicted velocity field. Then, a Poisson equation is constructed based on the divergence-free constraint (1) for the new time step and is solved to obtain the pressure field. Using the gradient of the pressure, the predicted velocity field is projected to the divergence-free space to obtain the velocity field for the new time step. The above process repeats at every time step in the simulation to advance the flow field in time in the LES. More details of numerical schemes used in the LES model can be found in Albertson[71] and Albertson and Parlange.[69]

III. MODEL VALIDATION

To validate the current LES-ALM model, we consider two different test cases. In the first test case, the LES model is applied to simulate the wake flow behind a laboratory-scale straight-bladed VAWT to reproduce the towing-tank experiment of Bachant and Wosnik.[16] In the second test case, the LES model is used to simulate the interaction between a straight-bladed VAWT and ABL turbulence to reproduce the LES results reported in Shamsoddin and Porté-Agel.[38] Details of these two validation cases are presented in Subsections III A and III B.

A. Towing-tank experiment validation case

The first validation case is designed to match the parameters of the towing-tank experiment in Bachant and Wosnik.[16] The VAWT in this case consists of three straight blades with a cross-sectional profile of a NACA0020 airfoil as well as a cylindrical center mast with a diameter of $D_{cm} = 0.095$ m. Each blade has a vertical height of $H = 1$ m, a chord length of $c = 0.14$ m, and a radial distance of $R = D/2 = 0.5$ m to the center axis of the VAWT. The dimensions of the simulation domain in the x-, y-, and z-directions are $L_x = 7.2$ m $= 7.2D$, $L_y = 3.7$ m $= 3.7D$, and $L_z = 2.7$ m $= 2.7D$, respectively. The inflow has a uniform streamwise mean velocity of $U_0 = 1$ m/s, and both the top and bottom boundaries are set to be free-slip to be compatible with this uniform inflow condition. The VAWT rotates counterclockwise at an angular speed of $\Omega = 3.8$ s^{-1}, which yields a turbine tip-speed ratio (TSR) of $\lambda = R\Omega/U_0 = 1.9$. The corresponding turbine rotor Reynolds number is $Re_D = U_0 D/\nu_w = 10^6$ and the blade chord Reynolds number[16] is $Re_c = \lambda U_0 c/\nu_w = 2.66 \times 10^5$, where the kinematic viscosity of water is $\nu_w = 1.0 \times 10^{-6}$ m^2/s at 20 °C.

The isotropic homogeneous turbulence dataset in the Johns Hopkins Turbulence Databases (JHTDB) is used to generate the turbulence fluctuations for the inflow condition based on the method developed by Martínez-Tossas *et al.*[50] Two different turbulent intensities are considered: $I_t \equiv \sqrt{2k/3}/U_0 = 0.03$ and 0.05, where $k = 0.5[(u'_{rms})^2 + (v'_{rms})^2 + (w'_{rms})^2]$ is the turbulent kinetic energy with $(u'_{rms}, v'_{rms}, w'_{rms})$ being the root mean square (rms) values for the fluctuations of the inflow velocity components. For the test run with $I_t = 0.05$, two different grid resolutions are considered: a lower resolution with $144 \times 72 \times 61$ grid points and a higher resolution with $288 \times 144 \times 61$ grid points. For the test run with $I_t = 0.03$, only the lower resolution with $144 \times 72 \times 61$ grid points is considered. These grid resolutions are chosen based on the LES tests of the same towing-tank experiment reported in Hezaveh *et al.*[14] For all three test cases, the width of the Gaussian kernel for the ALM is set to be $\varepsilon = 0.1$ m for the VAWT blades and $\varepsilon_{cm} = 0.05$ m for the center mast.

Figure 4 shows the comparison of the spanwise profiles of the time-averaged streamwise velocity at $1D$ downstream of the VAWT. The time average of the current LES results is computed based on 2000 instantaneous snapshots of the flow field sampled between $t = 24$ and 72 s. The time-averaged velocity profiles of all three test runs obtained using the current LES model show good agreement with the experimental data.[16] The current LES results agree with the LES result of Hezaveh *et al.*[14] for the overall magnitude and shape of the VAWT wake but show some discrepancy in the detailed wake profile in $-0.5 < y/D < 0.5$. This discrepancy may be caused by several differences in the details of simulation setups. For example, in Hezaveh *et al.*[14] the turbine-induced forces were distributed equally over five points spanning the chord length and further distributed to additional surrounding points with constant prescribed weights, while the current LES model uses a 3D Gaussian kernel to smoothly distribute the forces. Moreover, the Reynolds number used in the current LES matches with that reported in Bachant and Wosnik,[16] while Hezaveh *et al.*[14] used a chord Reynolds number of $Re_c = \lambda U_0 c/\nu_w = 5.7 \times 10^5$, which is about twice of the value reported in Bachant and Wosnik.[16] It is also unclear if the cylindrical center mast of the VAWT was considered in the LES of Hezaveh *et al.*[14] Nevertheless, the current LES results show overall good agreement with the experimental and LES data reported in the literature and low sensitivity to the grid resolution.

Note that the specific value of the inflow turbulence intensity was not reported in Hezaveh *et al.*[14] and Bachant and Wosnik.[16] As a reference, Shamsoddin and Porté-Agel[40] and Abkar and Dabiri[44] performed the LES of VAWT wake flow in water channel at a higher TSR of $\lambda = 3.85$ using an inflow turbulence intensity of 0.03. The two inflow turbulence intensities used in our LES model for the validation case are similar to that used in Shamsoddin and Porté-Agel[40] and Abkar and Dabiri.[44] As shown by the comparison in Fig. 4, the current LES model results are not sensitive to the choice of inflow turbulence intensity and both test cases (i.e., $I_t = 0.03$ and 0.05 with $144 \times 72 \times 61$ grid points) show good agreement with the reported experimental data. Note that if an even higher value of I_t is used for inflow, the stronger turbulent mixing of the inflow would enhance the wake recovery and also make the wake profile smoother. Nevertheless, considering the relatively low Reynolds number of the experiment in

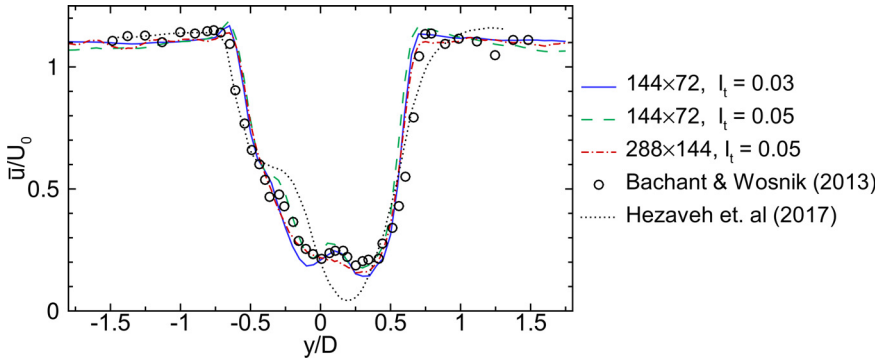

FIG. 4. Comparison of the spanwise profiles of the mean streamwise velocity at $(x - x_0) = 1D$ for the towing tank validation case, where x_0 is the streamwise location of the VAWT center axis. The towing tank experimental data points from Bachant and Wosnik[16] are denoted by the open circles. The LES result from Hezaveh *et al.*[14] obtained using $288 \times 144 \times 60$ grid points is denoted by the dotted line (black). The results obtained from the current LES model are denoted as follows: solid line (blue) for $I_t = 0.03$ with $144 \times 72 \times 61$ grid points; dashed line (green) for $I_t = 0.05$ with $144 \times 72 \times 61$ grid points; and dash-dot line (red) for $I_t = 0.05$ with $288 \times 144 \times 61$ grid points.

Bachant and Wosnik,[16] the relatively low turbulence intensities of $I_t = 0.03$ and 0.05 appear to be more reasonable choices for the current validation case than other higher values.

B. Atmospheric boundary layer flow validation case

The second validation case is configured based on the LES study of wind–VAWT interaction in a neutral ABL, as reported in Shamsoddin and Porté-Agel.[38] In this case, the VAWT consists of three straight blades with the cross-sectional shape of the NACA0018 airfoil. Each blade has a vertical height of $H = 100$ m and a chord length of $c = 2.4$ m. The turbine rotor diameter is $D = 2R = 50$ m, and the rotor equator (i.e., the middle height of the VAWT blades) is located at $z_{eq} = 100$ m above the ground. The VAWT rotates with a fixed TSR of $\lambda = R\Omega/U_{ref}$, where U_{ref} is the average of the instantaneous wind velocity sampled along the centerline at $1D$ upstream of the VAWT rotor region. In the current LES, the precursor simulation domain has a size of $(L_x^p, L_y, L_z) = (2400, 2400, 400)$ m and the main turbine simulation domain has a size of $(L_x, L_y, L_z) = (1600, 2400, 400)$ m $= (32D, 48D, 8D)$ (including a fringe zone of $4D$ long). The precursor and main turbine simulation domains are discretized using $384 \times 384 \times 385$ and $256 \times 384 \times 385$ grid points, respectively. The bottom boundary is flat and has a surface roughness of $z_0 = 0.1$ m. In the precursor simulation, the ABL flow is driven by a prescribed streamwise pressure gradient as shown in Eq. (3), and the corresponding wind friction velocity is $u_* = \sqrt{-(L_z/\rho)\mathrm{d}p_\infty/\mathrm{d}x} = 0.52$ m/s. The mean wind speed at the turbine equator height is about $U_{eq} = 9.49$ m/s. The width of the Gaussian kernel for the ALM is set to be $\varepsilon = 6.25$ m for the VAWT blades.

Note that the main simulation domain used in Shamsoddin and Porté-Agel[38] has a size of $(L_x, L_y, L_z) = (1200, 600, 400)$ m $= (24D, 12D, 8D)$, with only one VAWT included in this domain. As illustrated in Fig. 2, the ABL turbulence exhibits low- and high-speed streaks at different spanwise locations that can affect its interaction with the VAWT. If a narrow simulation domain is used, the single VAWT included in the simulation may operate in a low-speed streak for a considerable amount of time before the inflow evolves into a high-speed streak. As a result, a long simulation duration is required to obtain flow field samples for time average in order to eliminate the potential bias caused by the low- and high-speed streaks. In Shamsoddin and Porté-Agel,[38] the total physical time of the simulation was 90.4 min and the sampling time span for time average was 77.5 min. By contrast, the current LES uses a wider domain of $L_y = 2400$ m, which allows four VAWTs to be included in the LES. The four VAWTs are located at $x_0 = 200$ m $= 4D$ from the inflow boundary of the turbine simulation domain and are evenly spaced in the spanwise direction with a distance of $s_y = 600$ m $= 12D$. The ensemble average of the four VAWT sub-domains helps to obtain converged statistics with less simulation and sampling time required.

In the current LES test, the fully developed ABL turbulence initial condition was obtained by running the precursor simulation without the turbine simulation domain. The precursor LES was initialized based on the logarithmic mean velocity profile $U(z) = (u_*/\kappa)\ln(z/z_0)$ and random velocity fluctuations, where the von Kármán constant was set to be the typical value of $\kappa = 0.41$. Note that it can be computationally expensive to run the LES at high grid resolution from the initial random fluctuation state to the fully developed boundary layer turbulence state. To reduce the computational cost, the grid resolution of the LES was increased successively in three stages. The LES started at a low resolution with $128 \times 128 \times 129$ grid points and ran for 14 400 s with a time step of $\Delta t = 0.1$ s. Then, the simulation was interpolated to an intermediate resolution with $256 \times 256 \times 257$ grid points and was run for 4800 s with a time step of $\Delta t = 0.05$ s. After that, the simulation was interpolated to the high resolution with $384 \times 384 \times 385$ grid points and was run for 800 s with a time step of $\Delta t = 0.016$ s. After these three stages, the fully developed ABL turbulence was obtained and was also used to initialize the turbine simulation domain in the concurrent simulation. Finally, the concurrent precursor–main simulation was conducted using $384 \times 384 \times 385$ points for the precursor simulation domain and $256 \times 384 \times 385$ points for the main simulation domain (i.e., with identical grid resolution) for a total duration of 800 s. A time average was performed over 8200 three-dimensional instantaneous flow fields sampled within the last 648 s of the concurrent simulation with a time interval of about 0.079 s between each sample. The corresponding dimensionless values (i.e., normalized by D/U_{eq}) of the sampling duration and time interval are 123 and 0.015, respectively. Furthermore, as described previously, an ensemble average across the four simulated

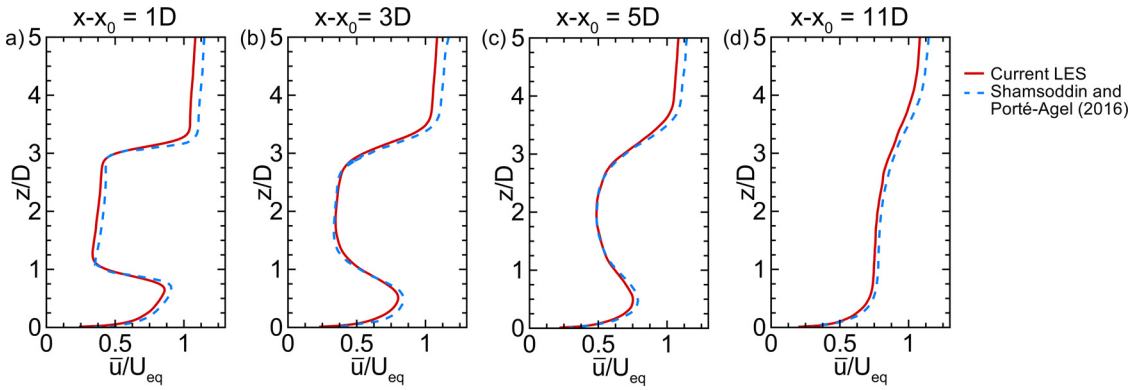

FIG. 5. Vertical profiles of mean streamwise velocity along the centerline of the turbine wake at different downstream locations $x - x_0 =$: (a) 1*D*; (b) 3*D*; (c) 5*D*; and (d) 11*D*. The results obtained from the current LES study are shown by the red solid lines, and those from Ref. 38 are shown by the blue dashed lines.

turbines was also performed. Hereinafter, the time- and turbine-averaged value of a physical quantity f is referred to as its "mean" value and denoted as $\bar{f}$.

Figures 5 and 6 show the vertical and spanwise profiles of the mean streamwise velocity at four different downstream locations of the turbine wake. The rotating VAWTs generate a significant velocity deficit in the near-wake region, which recovers gradually toward the downstream direction due to the turbulent mixing. The mean velocity profiles obtained from the current LES mode show good agreement with the results reported Ref. 38, indicating that the current LES model captures the interaction of the straight-bladed VAWT with the ABL wind turbulence correctly.

IV. LES OF HELICAL-SHAPED VAWT IN THE BOUNDARY LAYER TURBULENCE

A. Setup of LES cases

In this section, we apply the LES model to simulate the effect of helical-shaped blades on the wake flow characteristics of VAWTs operating in the boundary layer turbulence. One straight-bladed VAWT and two helical-bladed VAWTs are considered in order to investigate the effects of helical blade shape on the wake flow characteristics. All three VAWTs have identical key parameters except for the blade shape. In particular, each VAWT consists of three blades with the cross-sectional shape of the NACA0018 airfoil. Each blade has a vertical height of $H = 3.2$ m and a chord length of $c = 0.511$ m. The turbine rotor diameter is $D = 2R = 1.8$ m, and the rotor equator is at $z_{eq} = 8.2$ m above the ground (i.e., $z_{eq}/D \approx 4.56$). In the LES, all three VAWT models rotate counterclockwise at the same fixed TSR of $\lambda = R\Omega/U_{ref} = 1.19$. For a helical-shaped VAWT, taking the top end as the reference, if the blades are twisted counterclockwise (i.e., in the same direction as the turbine rotation direction) toward the bottom end, the twist angle γ between the top and bottom edges is defined to be positive. In this study, two helical-bladed VAWTs with opposite twist angles $\gamma = \pm 127^\circ$ are considered. The corresponding blade twist rate is 39.69° per meter height. Note that the $\gamma = -127^\circ$ helical-bladed VAWT considered in the current LES study is analogous to the commercial VAWT studied by Wei *et al.*,[22] except that the orientation and direction of rotation of the turbine are both mirrored, and the cross-sectional profile of the blades do not match precisely. The commercial helical-bladed VAWT does not use a standard cross-sectional aerodynamic profile, and thus, the lift and drag coefficients are not available for modeling purposes.

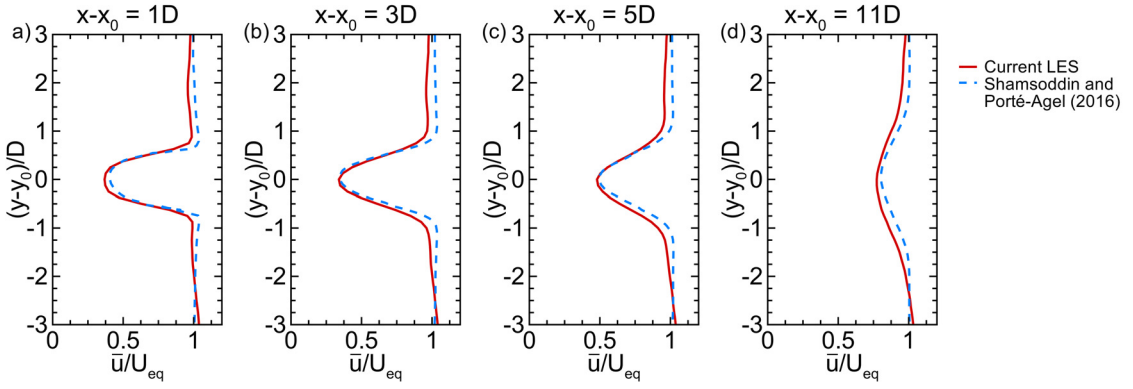

FIG. 6. Spanwise profiles of mean streamwise velocity at the equator height at different downstream locations $x - x_0 =$: (a) 1*D*, (b) 3*D*, (c) 5*D*, and (d) 11*D*. The results obtained from the current LES study are shown by the red solid lines, and those from Ref. 38 are shown by the blue dashed lines.

Nevertheless, the effects of the VAWT helical geometry on the wake flow characteristics are expected to be similar, despite the difference in the blade cross-sectional profile.

For the LES cases reported in this section, the precursor simulation domain has a size of $(L_x^p, L_y, L_z) = (80, 80, 20)$ m and the main turbine simulation domain has a size of $(L_x, L_y, L_z) = (60, 80, 20)$ m $= (33.33D, 44.44D, 11.11D)$ (including a fringe zone of $4.167D$ long, i.e., 1/8 of the total domain length). The precursor and main turbine simulation domains are discretized using $512 \times 512 \times 289$ and $384 \times 512 \times 289$ grid points, respectively. The bottom boundary surface roughness is $z_0 = 0.01$ m. In the precursor simulation, the boundary layer turbulence is driven by a prescribed streamwise pressure gradient as shown in Eq. (3), and the corresponding wind friction velocity is $u_* = 0.64$ m/s. The inflow and initial conditions are also generated using a similar strategy as that used for the ABL condition validation case reported in Sec. III B. The mean wind speed at the turbine equator height obtained from the precursor simulation is about $U_{eq} = 11.79$ m/s. As in the ABL condition validation case shown in Sec. III B, in each simulation case there are four identical VAWTs included in the main turbine simulation domain at $x_0 = 7.2$ m $= 4D$, with an even spanwise spacing of $s_y = 20$ m $= 11.11D$. The width of the Gaussian kernel for the ALM is set to be $\varepsilon = 0.16$ m for the VAWT blades.

The LES started at a low resolution with $64 \times 64 \times 97$ grid points and ran for 2750 s with a time step of $\Delta t = 4 \times 10^{-3}$ s. Then, the simulation was interpolated to an intermediate resolution with $256 \times 256 \times 193$ grid points and ran for 370 s with a time step of $\Delta t = 2 \times 10^{-3}$ s. After that, the simulation was interpolated to the high resolution with $512 \times 512 \times 289$ grid points and ran for another 210 s with a time step of $\Delta t = 6.25 \times 10^{-4}$ s. After these three stages, the fully developed boundary layer turbulence was obtained and used to also initialize the turbine simulation domain in the concurrent simulation. A time average was obtained across 4500 three-dimensional instantaneous flow fields sampled within the last 56.25 s of the concurrent simulation with a time interval of about 0.0125 s between each sample. The time-averaged flow statistics are presented below in the Subsections IV C–IV F.

B. Instantaneous flow fields

Figures 7–9 show the instantaneous velocity fields for the cases with the straight-bladed VAWT, −127°helical-bladed VAWT, and 127° helical-bladed VAWT, respectively. In particular, the (x, z)-plane across the center of one VAWT and the (x, y)-plane at its equator height are shown for each case, with the origin of the horizontal coordinates shifted to the turbine center (x_0, y_0). In the straight-bladed VAWT case, the rotating blades induce periodic fluctuations to the streamwise and spanwise velocities in vertical streak patterns in the near-wake region (i.e., $x - x_0 \lesssim 4D$) [Figs. 7(a) and 7(c)]. In this near-wake region, the vertical velocity fluctuation is much more intensive in the two distinct shear layers at the top and bottom edges of the turbine wake than near the equator height [Figs. 7(e) and 7(f)]. Further downstream (i.e., $x - x_0 > 4D$), the blade-induced coherent flow structures break down and the wake transitions to fully turbulent, as indicated by the strong spanwise and vertical velocity fluctuations that can be seen in both the (x, z)- and (x, y)-plane views [Figs. 7(c)–7(f)]. The turbulent mixing associated with these fluctuations helps enhance the

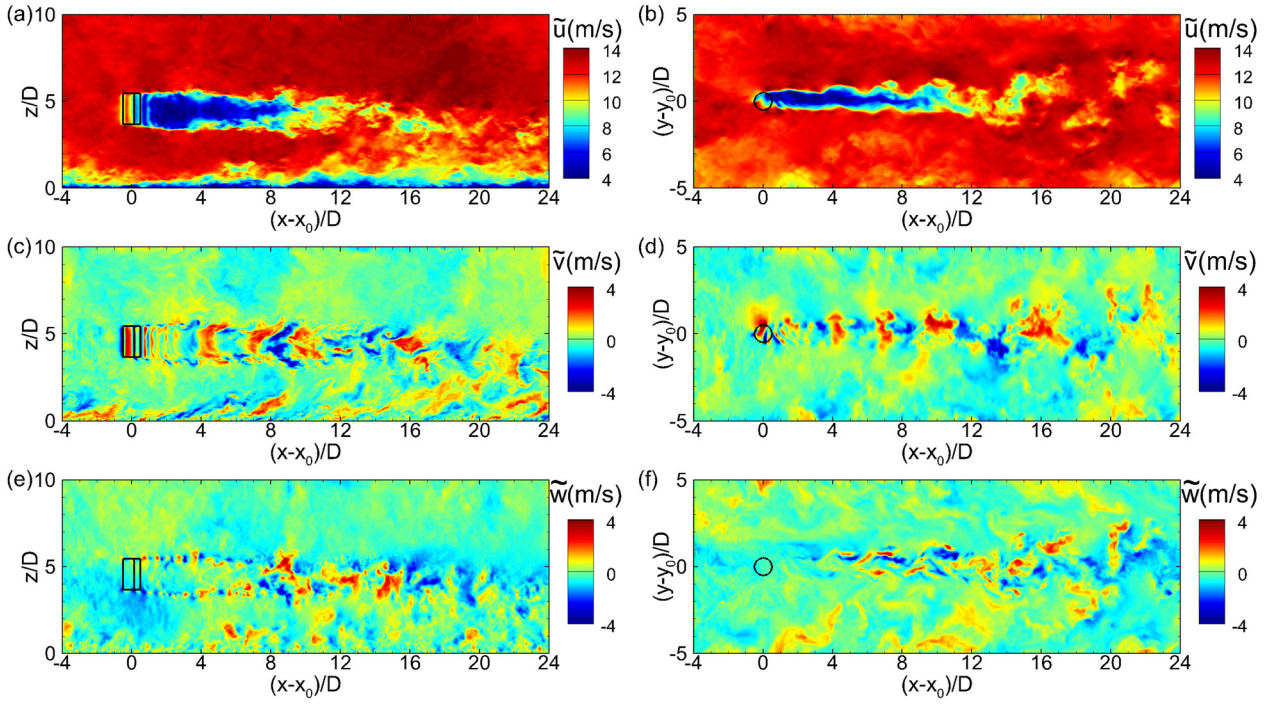

FIG. 7. Instantaneous velocity fields in the boundary layer turbulence around the straight-bladed VAWT: (a) and (b) streamwise velocity $\tilde{u}$; (c) and (d) spanwise velocity $\tilde{v}$; (e) and (f) vertical velocity $\tilde{w}$. The left panels show the (x, z)-plane across the center of the VAWT, and the right panels show the (x, y)-plane at the VAWT equator height.

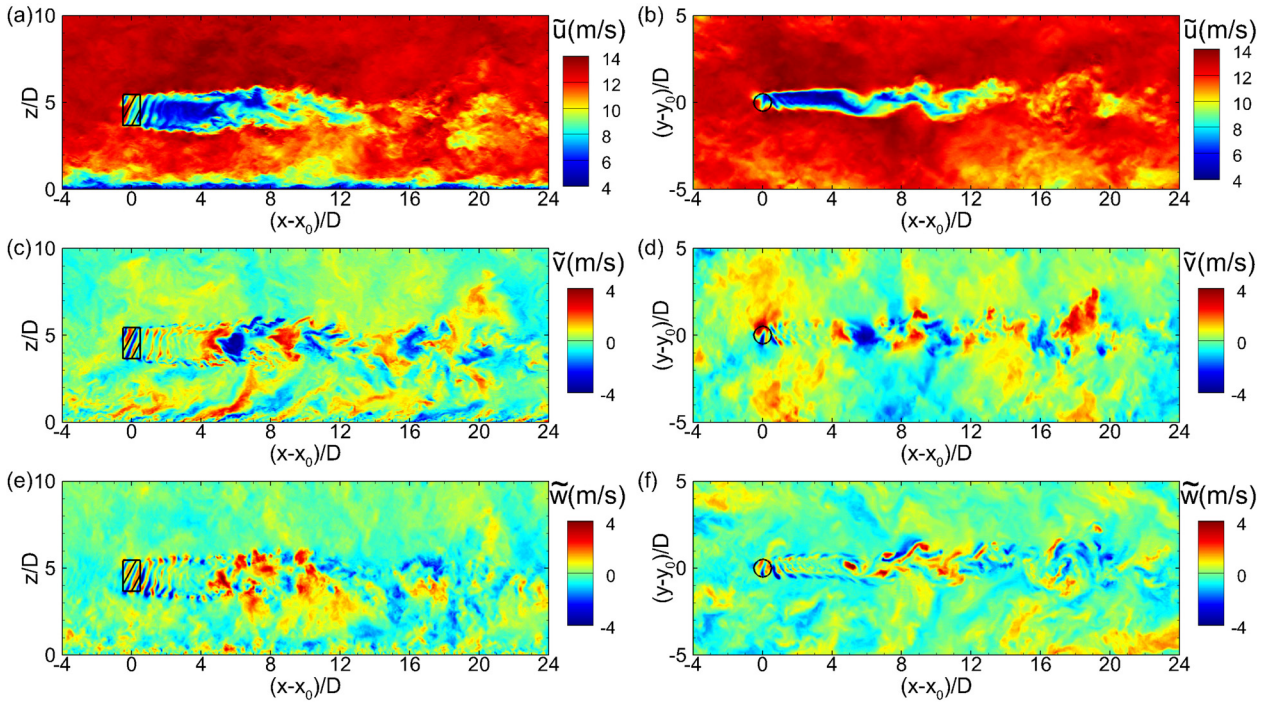

FIG. 8. Instantaneous velocity fields in the boundary layer turbulence around the helical-bladed VAWT with $\gamma = -127°$: (a) and (b) streamwise velocity $\tilde{u}$; (c) and (d) spanwise velocity $\tilde{v}$; (e) and (f) vertical velocity $\tilde{w}$. The left panels show the (x, z)-plane across the center of the VAWT, and the right panels show the (x, y)-plane at the VAWT equator height.

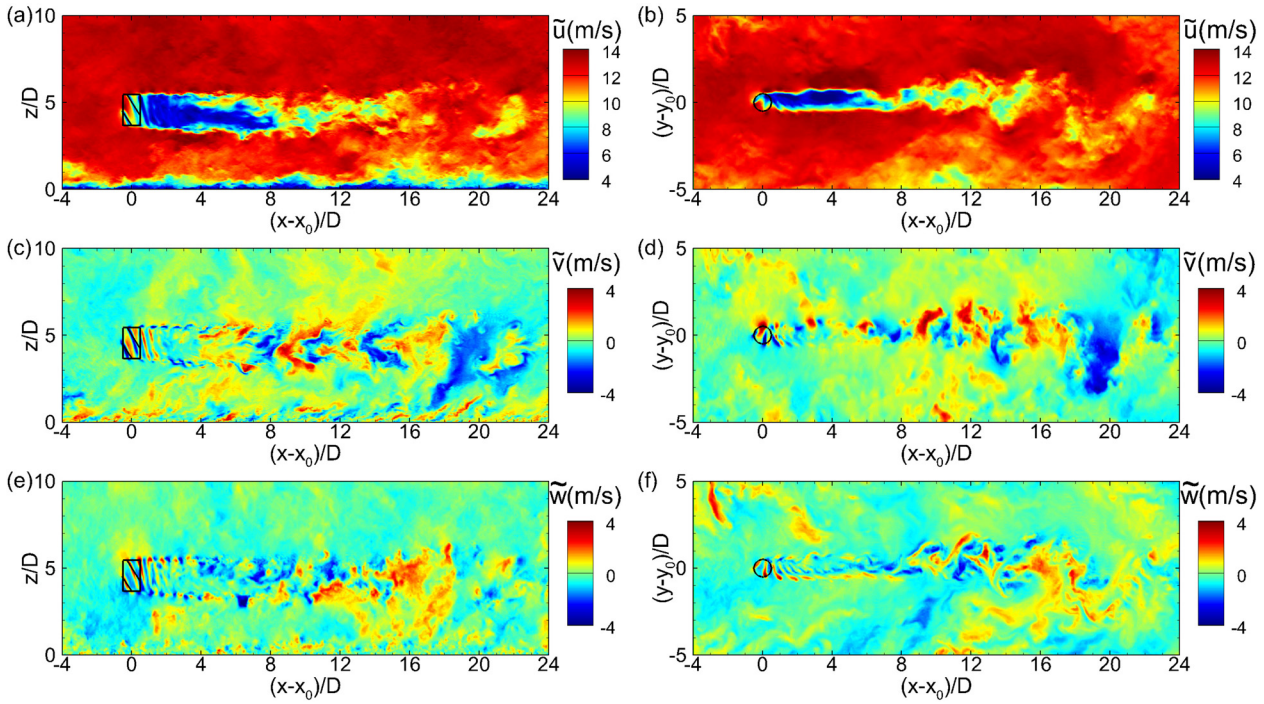

FIG. 9. Instantaneous velocity fields in the boundary layer turbulence around the helical-bladed VAWT with $\gamma = 127°$: (a) and (b) streamwise velocity $\tilde{u}$; (c) and (d) spanwise velocity $\tilde{v}$; (e) and (f) vertical velocity $\tilde{w}$. The left panels show the (x, z)-plane across the center of the VAWT, and the right panels show the (x, y)-plane at the VAWT equator height.

recovery of the streamwise velocity as the wake flow moves downstream ($x - x_0 \gtrsim 6D$).

The effects of the helical-shaped blades on the instantaneous velocities are more noticeable in the near-wake region (i.e., $x - x_0 \lesssim 4D$) than in the far wake. Taking the helical-bladed VAWT with $\gamma = -127^\circ$ as an example, the helical shape of the rotating blades causes the streak patterns of the streamwise and spanwise velocity fluctuations to be inclined with respect to the vertical direction [Figs. 8(a) and 8(c)]. In the near-wake region, the helical blades also induce more vertical velocity fluctuations in the middle region between the top and bottom shear layers [Figs. 8(e) and 8(f)] than that in the straight-bladed VAWT case. Moreover, a close-up look at the near-wake region in Fig. 8(f) shows that the $\gamma = -127^\circ$ helical blades generate downward flow motions around $y - y_0 \approx \pm 0.5D$, which are accompanied by upward counter-flow motions in the middle of the wake around $y - y_0 = 0$. The 3D view of this near-wake vertical flow pattern is shown in Fig. 10(b), with the straight-bladed case shown in Fig. 10(a) for comparison. If the twist direction of the helical blades is reversed, Fig. 9 shows that the $\gamma = 127^\circ$ helical-bladed VAWT generates similar effects to the turbine wake flow, but with the inclination direction of the streamwise and spanwise velocity fluctuations as well as the sign of the vertical velocity fluctuations in the near-wake region reversed compared with those in the $\gamma = -127^\circ$ case.

C. Time-averaged flow fields

Figure 11 shows the planar views of the time-averaged vertical velocity in the wakes of the straight- and helical-bladed VAWTs. Here, the straight-bladed VAWT case [Figs. 11(c) and 11(d)] can be used as the baseline case to help understand the averaged effect of the helical blades on the vertical motions of the wake flow. As the boundary layer turbulence inflow approaches the turbine, the blockage effect of the rotating blades forces some of the inflow to bypass the rotor, resulting in the positive and negative $\bar{w}$ around the top and bottom ends of the VAWT rotor, respectively [Fig. 11(c)]. After passing the VAWT, the flow moves toward the center of the wake from top and bottom, with the upward velocity at the bottom edge of the wake region stronger than the downward velocity at the top edge. This net upward flow in the wake is balanced by the downward flow next to the wake [i.e., the slightly negative $\bar{w}$ at $-4 \lesssim (y - y_0)/D \lesssim -1$ in Fig. 11(d)].

As indicated by the instantaneous flow results in Sec. IV B, the helical-shaped blades in the $\gamma = -127^\circ$ case push the flow downwards, causing an upward counter flow to be generated at the center of the turbine wake. This effect can also be seen clearly in Figs. 11(a) and 11(b) in the time-averaged $\bar{w}$ field, where the two negative $\bar{w}$ regions in the near wake correspond to the downward flows induced directly by the forcing from the $\gamma = -127^\circ$ helical blades and the noticeable positive $\bar{w}$ around the centerline of the near-wake region correspond to the upward counter flow. Consistent with the instantaneous flow results, the time-averaged results for $\bar{w}$ also show that reversing the blade twist direction causes the blade-induced effects on the vertical flow motions to be reversed [Figs. 11(e) and 11(f)]. To show the net effect of the helical-shaped blades on the mean vertical motions of the wake flow, the difference of the mean vertical velocity between the two helical-bladed VAWT cases and the straight-bladed VAWT case are calculated. In particular, for each helical-bladed VAWT case the difference is calculated as $\Delta\bar{w}(x, y, z) = \bar{w}(x, y, z) - \bar{w}_s(x, y, z)$, where $\bar{w}_s(x, y, z)$ is the time-averaged vertical velocity for the straight-bladed VAWT case [Figs. 11(c) and 11(d)]. As shown in Fig. 12, the contours of $\Delta\bar{w}$ in the wakes of the two helical-bladed VAWTs exhibit similar magnitudes but with reversed signs. A similar effect on the mean vertical motion of the wake flow induced by the helical-bladed VAWT has also been reported in the experimental study by Wei *et al.*[22] and RANS modeling by Divakaran *et al.*[28]

Due to the mean vertical motions induced by the helical blades, the wake flow behind helical-bladed VAWT is inclined in the vertical direction. The left column of Fig. 13 shows the 2D contours of $\bar{u}$ on the (x, z)-plane across the turbine center axis for the three VAWT cases, and Fig. 14 shows the corresponding vertical profiles of $\bar{u}$ at different streamwise locations. Compared with the straight-bladed VAWT case, the wake of the VAWT with $\gamma = -127^\circ$ is inclined upward while the wake in the $\gamma = 127^\circ$ case is inclined downward. The streamwise velocity deficits in the two helical-bladed VAWT cases have slightly smaller magnitudes than that in the straight-bladed VAWT case in the near-wake region $x - x_0 \lesssim 5D$ [Figs. 14(a)–14(c)]. The difference in the velocity deficit becomes less significant as the wake extends further downstream. In the far wake at $x - x_0 \gtrsim 11D$ [Figs. 14(f) and 14(g)], the vertical profiles of $\bar{u}$ in the straight-bladed and $\gamma = -127^\circ$ helical-bladed VAWT cases almost overlap with each other, while $\bar{u}$ in the $\gamma = 127^\circ$ helical-bladed VAWT case exhibits a slightly smaller value at $2 \lesssim z/D \lesssim 5$. The horizontal patterns of $\bar{u}$ at

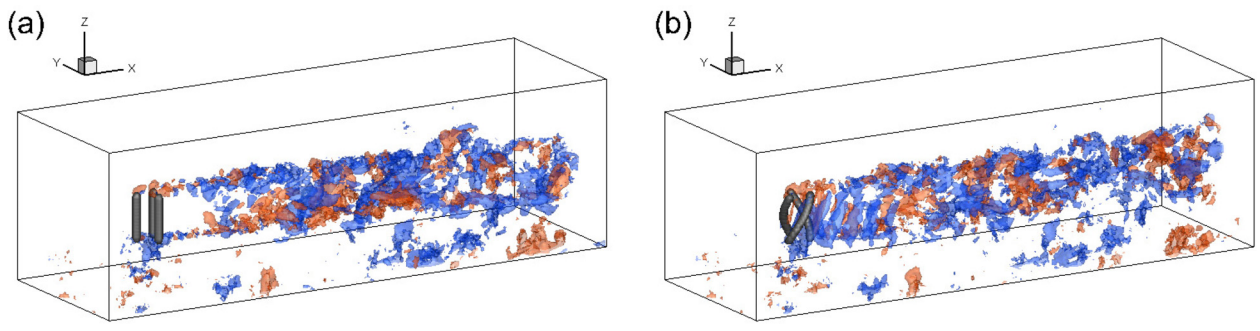

FIG. 10. Instantaneous vertical velocity fields in the wakes downstream of the (a) straight-bladed and (b) helical-bladed VAWTs with $\gamma = -127^\circ$. The red and blue colored iso-surfaces represent $\tilde{w} = 1.5$ m/s and $\tilde{w} = -1.5$ m/s, respectively. The VAWT blades are visualized using iso-surfaces (dark gray color) of the 3D Gaussian kernel (for distributing the turbine blade forces).

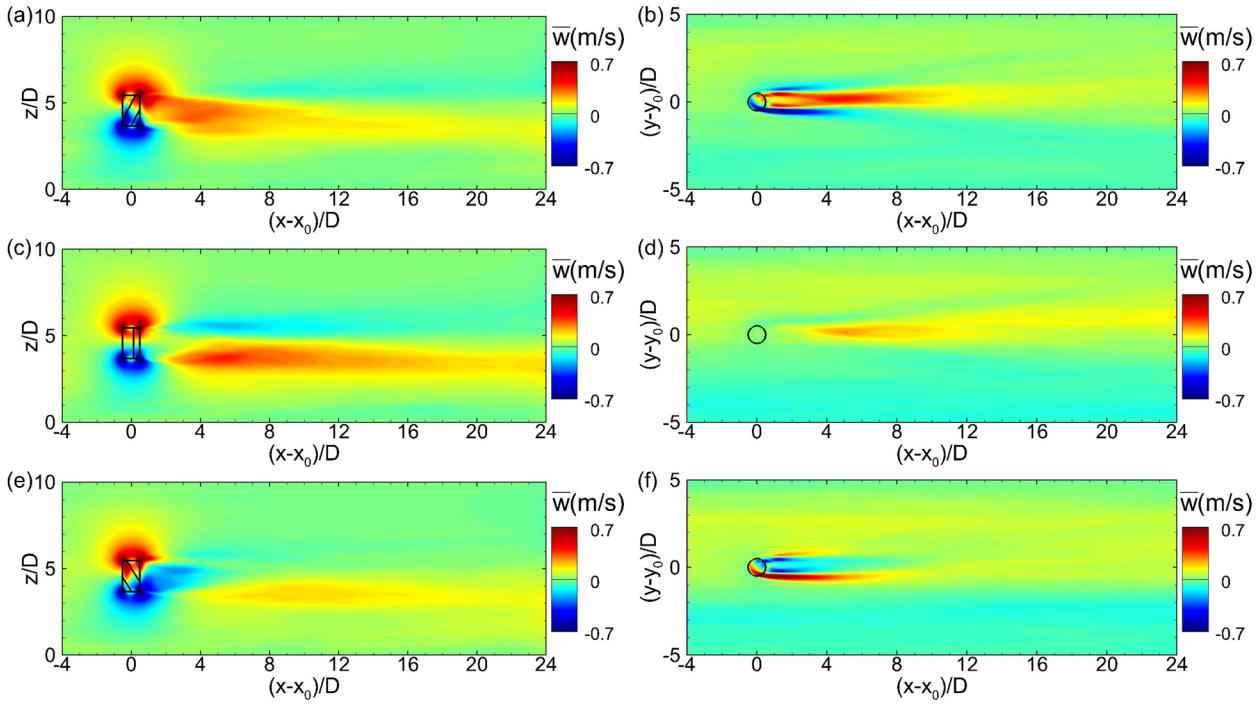

FIG. 11. Time-averaged vertical velocity $\bar{w}$ on the (x, z)-plane across the center axis of the VAWT (left column) and on the (x, y)-plane at the equator height (right column): (a) and (b) helical-bladed VAWT with $\gamma = -127^\circ$; (c) and (d) straight-bladed VAWT; (e) and (f) helical-bladed VAWT with $\gamma = 127^\circ$.

the equator height in the two helical-bladed VAWT cases are similar to that in the straight-bladed case [Figs. 13(b), 13(d), 13(f), and 15], except for the slightly higher magnitude of streamwise velocity deficit in the straight-bladed VAWT case in the near-wake region [Figs. 15(a)–15(c)].

To quantify the effect of helical-shaped blades on the wake inclination, we define the wake center height at each streamwise location x as

$$Z_c(x) = \frac{\int_{A_w} [\bar{u}(x,y,z) - \bar{u}(x_{in},y,z)]z\,\mathrm{d}A}{\int_{A_w} [\bar{u}(x,y,z) - \bar{u}(x_{in},y,z)]\mathrm{d}A}, \tag{19}$$

where $\bar{u}(x_{in},y,z)$ is the time-averaged streamwise velocity at the inlet $x = x_{in}$ of the turbine simulation domain and A_w is the turbine wake cross-section identified based on the condition

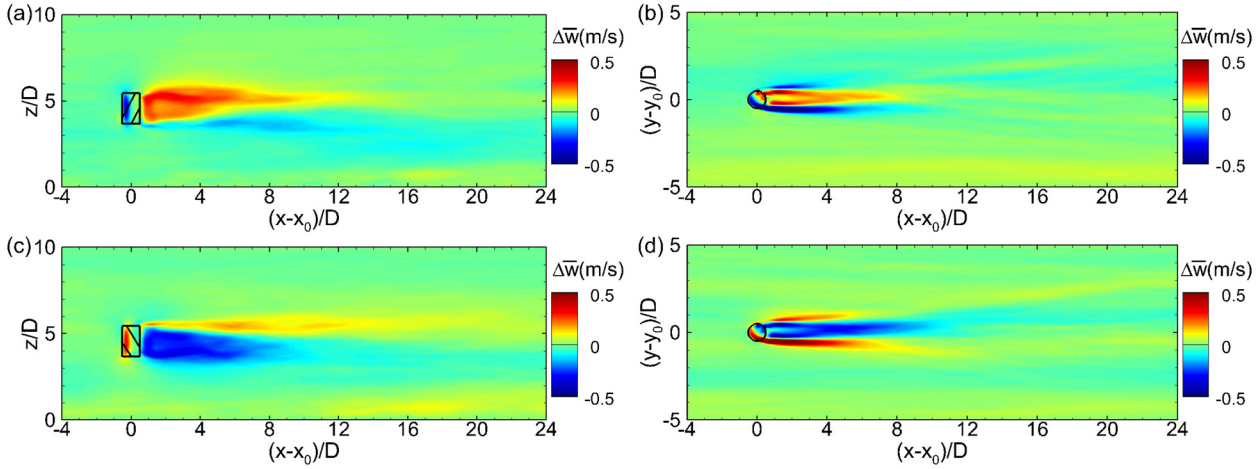

FIG. 12. Differences in the time-averaged vertical velocity relative to the straight-bladed VAWT case: (a) and (b) helical-bladed VAWT with $\gamma = -127^\circ$; (c) and (d) helical-bladed VAWT with $\gamma = 127^\circ$.

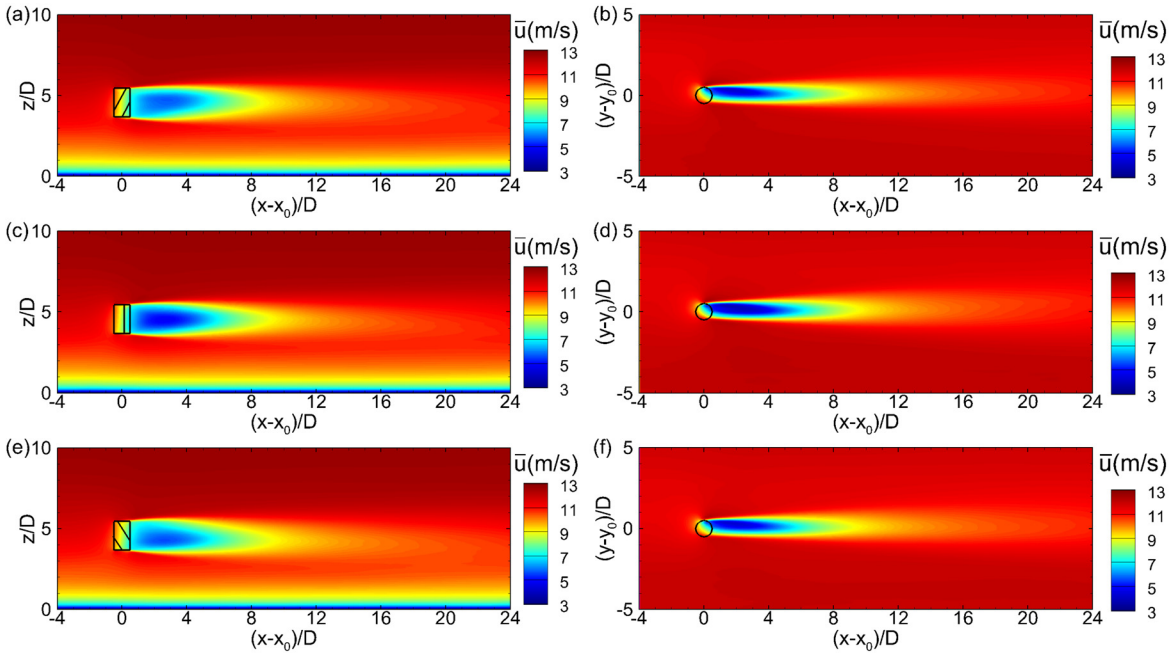

FIG. 13. Time-averaged streamwise velocity $\bar{u}$ on the (x, z)-plane across the center axis of the VAWT (left column) and on the (x, y)-plane at the rotor equator height (right column): (a) and (b) helical-bladed VAWT with $\gamma = -127^{\circ}$; (c) and (d) straight-bladed VAWT; (e) and (f) helical-bladed VAWT with $\gamma = 127^{\circ}$.

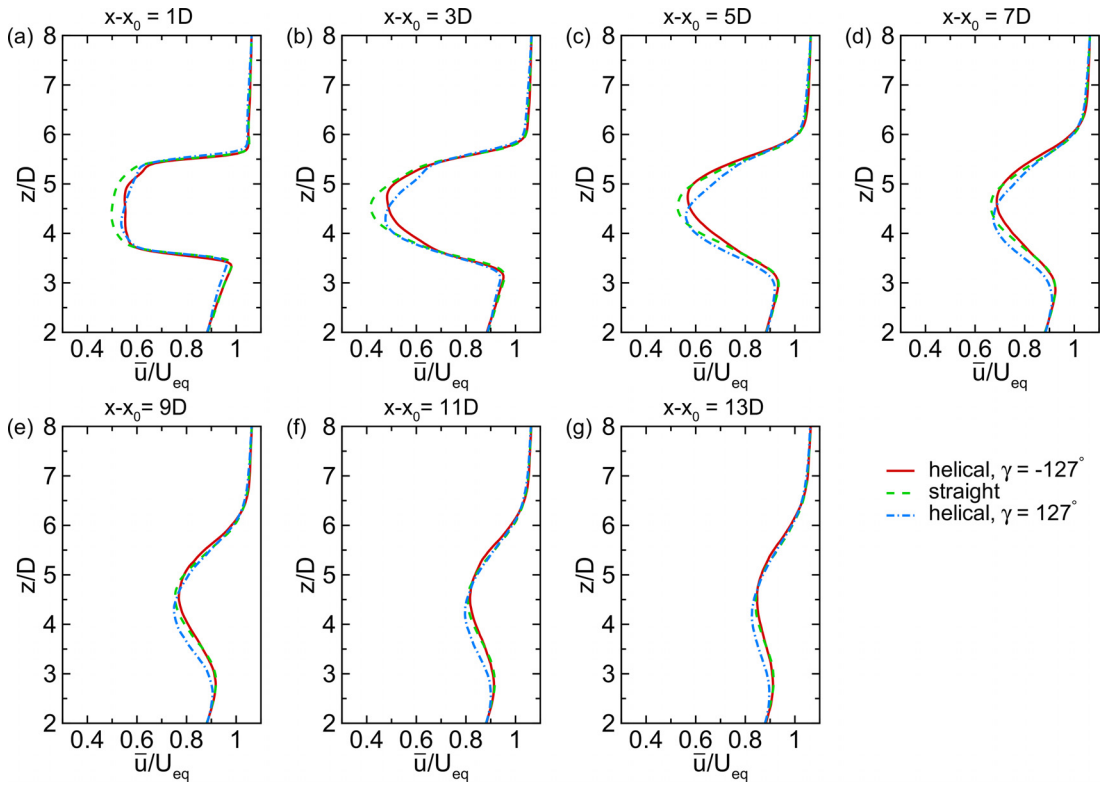

FIG. 14. Vertical profiles of $\bar{u}$ along the wake centerline at different streamwise locations $(x - x_0) =$: (a) 1D; (b) 3D; (c) 5D; (d) 7D; (e) 9D; (f) 11D; and (g) 13D. Solid lines: helical VAWT with $\gamma = -127^{\circ}$; dashed lines: straight VAWT; dash-dot lines: helical VAWT with $\gamma = 127^{\circ}$.

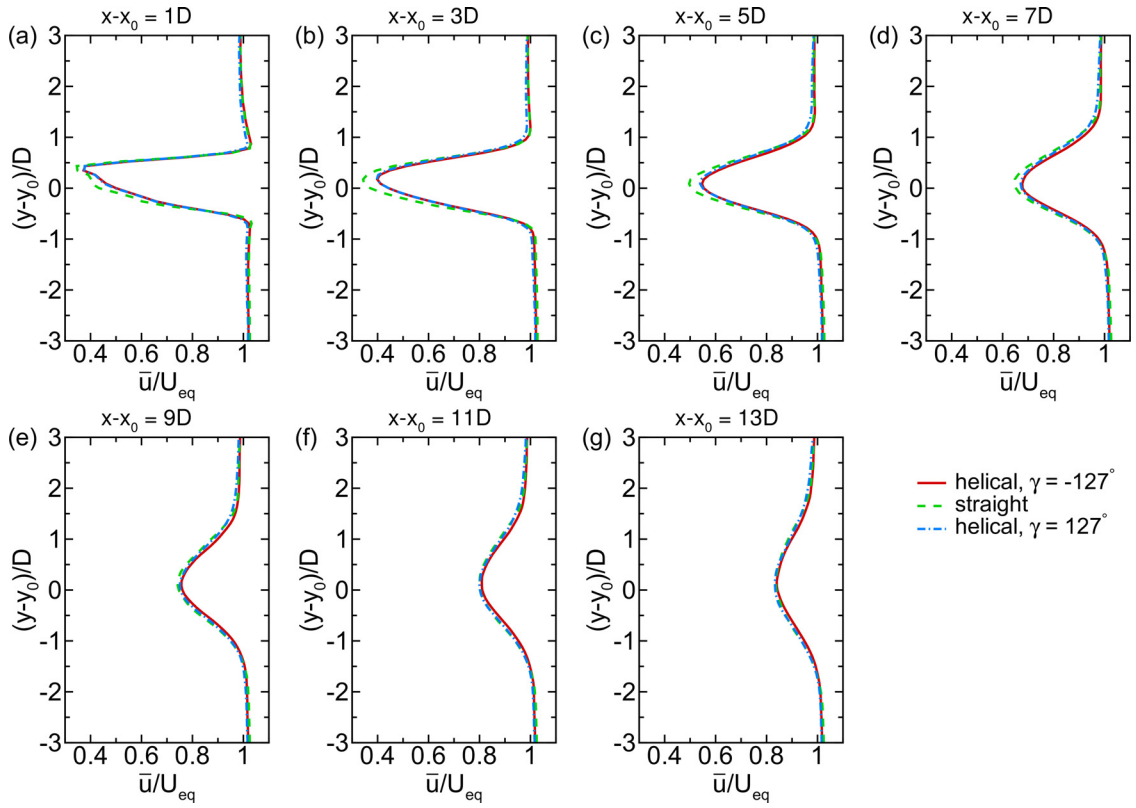

FIG. 15. Spanwise profiles of $\bar{u}$ at the turbine equator height at different streamwise locations $(x - x_0) =$: (a) 1*D*; (b) 3*D*; (c) 5*D*; (d) 7*D*; (e) 9*D*; (f) 11*D*; and (g) 13*D*. Solid lines: helical-bladed VAWT with $\gamma = -127°$; dashed lines: straight-bladed VAWT; dash-dot lines: helical-bladed VAWT with $\gamma = 127°$.

$\bar{u}(x, y, z) - \bar{u}(x_{in}, y, z) < 0$. This definition of Z_c is analogous to that for the center of mass height of an object. Figure 16 compares $Z_c(x)$ for the three cases. For the straight-bladed VAWT case, Z_c starts with a value that is very close to the turbine equator height z_{eq}, and increases gradually with x due to the turbulent mixing between the low-speed wake region and the high-speed free-stream wind above the wake. For comparison, the mean upward motion of the wake flow in the $\gamma = -127°$ case [Figs. 12(a) and 12(b)] causes

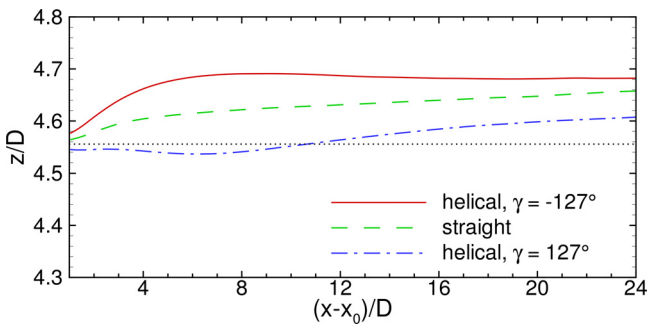

FIG. 16. Streamwise variation of turbine wake center height Z_c as defined in Eq. (19). The turbine equator height z_{eq} is also shown by the dotted line as a reference height.

Z_c to increase much more rapidly than that in the straight-bladed VAWT case, resulting in a higher wake center height. In the $\gamma = 127°$ case, the mean downward motion of the wake flow overcomes the upward shift effect caused by the turbulent mixing between the free-stream wind and the wake flow, causing Z_c to slightly decrease and become smaller than z_{eq} at $1 \lesssim (x - x_0)/D \lesssim 10$. At $(x - x_0)/D > 10$, the downward motion of the wake flow in the $\gamma = 127°$ case becomes too weak [Figs. 12(c) and 12(d)], and Z_c increases to be above z_{eq} due to the effect of turbulent mixing. More analyses and discussions for the turbulent mixing in the turbine wake region are given in Sec. IV E.

Despite the vertical inclination, the magnitude of the turbine wake does not exhibit significant difference between the straight- and helical-bladed VAWT cases, suggesting that the effect of helical blades on the power production rate may be small for the flow condition and blade twist angles considered in the present study. To confirm this, the mean power coefficient for each case is calculated based on $C_p = P/(0.5\rho HDU_{10}^3)$, where P is the mean power (averaged in time and among the four turbines in each case) and U_{10} is the magnitude of the mean inflow velocity at 10 m reference height.[22] For the three cases considered here, the corresponding mean power coefficients are $C_p = 0.0627$, 0.0605, and 0.0622 for $\gamma = -127°$, straight-bladed, and $\gamma = 127°$ VAWTs, respectively. These values fall well within the range of the measured power coefficients reported in Wei *et al.*[22] (see their Fig. 3).

D. Time-averaged statistics of turbulent fluctuations of the VAWT wake flow

The LES results shown in Secs. IV B and IV C suggest that the helical-shaped blades can affect the turbulent fluctuations in the wake flow by direct disturbance as well as by inclining the wake region vertically. In this section, these effects are quantified by calculating the time-averaged statistics of the VAWT wake flow.

Figure 17 shows the distribution of the streamwise velocity variance $\overline{u'u'}$ on the (x, z)-plane across the VAWT center and on the (x, y)-plane at the equator height. The corresponding vertical and spanwise profiles at various streamwise locations are shown in Figs. 18 and 19, respectively. In the straight-bladed VAWT case [Figs. 17(c) and 17(d)], $\overline{u'u'}$ exhibits high intensity in the four shear layers extending from $x - x_0 \approx 1D$ to $8D$ surrounding the wake due to the shear instability, but low intensity around the middle of the wake right behind the turbine at $1D \lesssim x - x_0 \lesssim 4D$ [Figs. 18(a) and 18(b)]. Beyond $x - x_0 \approx 8D$, the four shear layers merge and the magnitude of $\overline{u'u'}$ is reduced due to turbulent dissipation. In the case of helical-bladed VAWT with $\gamma = -127°$, the upward inclination of the wake (Fig. 13) causes the magnitude of $\partial\bar{u}/\partial z$ to be decreased in the lower shear layer, resulting in the reduction of $\overline{u'u'}$ there [Figs. 17(a) and 18(c)–18(g)]. Reversing the twist angle to $\gamma = 127°$ causes the effect on $\overline{u'u'}$ to be reversed, i.e., weakened $\overline{u'u'}$ in the upper shear layer [Figs. 17(e) and 18(c)–18(g)]. In both helical-bladed VAWT cases, the streamwise turbulent fluctuation is enhanced in the middle of the near-wake region (i.e., at $1D \lesssim x - x_0 \lesssim 4D$) due to the direct velocity disturbance induced by the helical-shaped blades. The horizontal distribution of $\overline{u'u'}$ is similar for the three cases [Figs. 17(b), 17(d), and 17(e)], except that the peak values in the two horizontal shear layers for the helical-bladed VAWT cases are slightly lower than that for the straight-bladed VAWT case [Figs. 19(b)–19(d)].

Figure 20 shows the distribution of the vertical velocity variance $\overline{w'w'}$ on the (x, z)-plane across the VAWT center and on the (x, y)-plane at the equator height. The corresponding vertical and spanwise profiles at various streamwise locations are shown in Figs. 21 and 22, respectively. Consistent with the direct observation of the instantaneous vertical velocity fields [Figs. 8(e), 8(f), 9(e), and 9(f)], the helical-shaped turbine blades induce considerable vertical velocity fluctuations in the turbine-rotor region and in the near-wake region (i.e., $-0.5D \lesssim x - x_0 \lesssim 2D$) [Figs. 20, 21(a), and 22(a)]. At $x - x_0 \gtrsim 5D$, the upward inclination of the wake in the $\gamma = -127°$ VAWT case [Fig. 20(a)] weakens the lower shear layer, resulting in the reduction of $\overline{w'w'}$ there. Reversing the blade twist angle to $\gamma = 127°$ causes the effect of the helical-shaped blades on $\overline{w'w'}$ to be also reversed [Fig. 20(e)]. Unlike $\overline{u'u'}$, the high-intensity region of $\overline{w'w'}$ extends over a long streamwise distance, where the reduction of $\overline{w'w'}$ caused by the helical-shaped blades can be observed consistently throughout the range $5D \lesssim x - x_0 \lesssim 13D$ [Figs. 20, 21(c)–21(g), and 22(c)–22(g)].

E. Turbulent transport in the turbine wake

The effects of the helical-shaped blades on the wake turbulence can affect the turbulence-induced mixing and transport in the wake. In this section, the statistics of the LES-resolved Reynolds stresses $\overline{u'w'}$ and $\overline{u'v'}$ as well as the unresolved SGS shear stresses $\bar{\tau}_{zx}$ and $\bar{\tau}_{yx}$ are studied. In particular, $\overline{u'w'}$ and $\bar{\tau}_{zx}$ represent the resolved and unresolved (SGS) turbulent transport of streamwise momentum along the

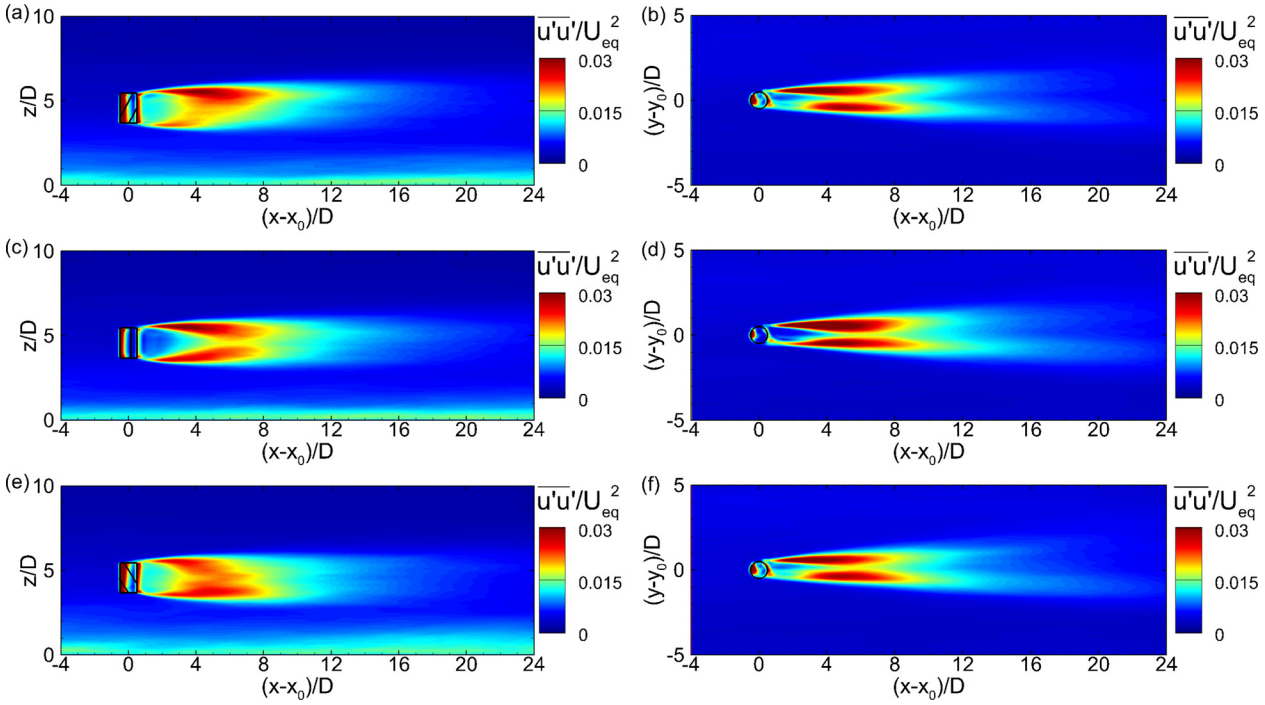

FIG. 17. Streamwise velocity variance $\overline{u'u'}$ on the (x, z)-plane across the center axis of the VAWT (left column) and on the (x, y)-plane at the equator height (right column): (a) and (b) helical-bladed VAWT with $\gamma = -127°$; (c) and (d) straight-bladed VAWT; (e) and (f) helical-bladed VAWT with $\gamma = 127°$.

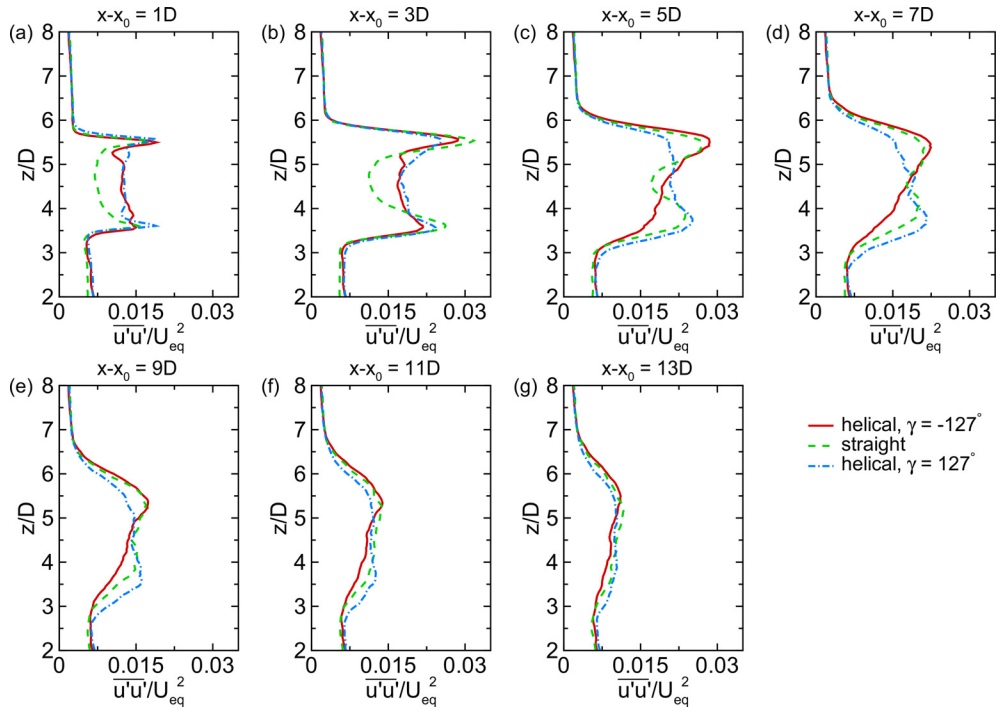

FIG. 18. Vertical profiles of $\overline{u'u'}$ along the wake centerline at different streamwise locations $(x - x_0) =$: (a) 1*D*; (b) 3*D*; (c) 5*D*; (d) 7*D*; (e) 9*D*; (f) 11*D*; and (g) 13*D*. Solid lines: helical-bladed VAWT with $\gamma = -127°$; dashed lines: straight-bladed VAWT; dash-dot lines: helical-bladed VAWT with $\gamma = 127°$.

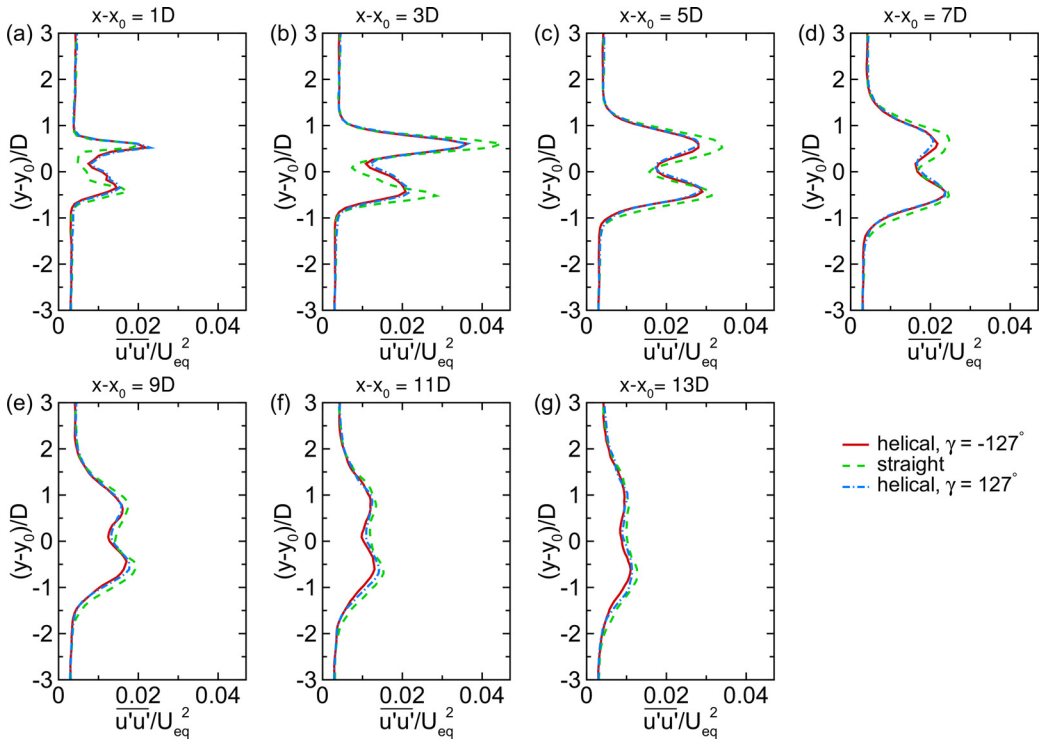

FIG. 19. Spanwise profiles of $\overline{u'u'}$ at the turbine equator height at different streamwise locations $(x - x_0) =$: (a) 1*D*; (b) 3*D*; (c) 5*D*; (d) 7*D*; (e) 9*D*; (f) 11*D*; and (g) 13*D*. Solid lines: helical-bladed VAWT with $\gamma = -127°$; dashed lines: straight-bladed VAWT; dash-dot lines: helical-bladed VAWT with $\gamma = 127°$.

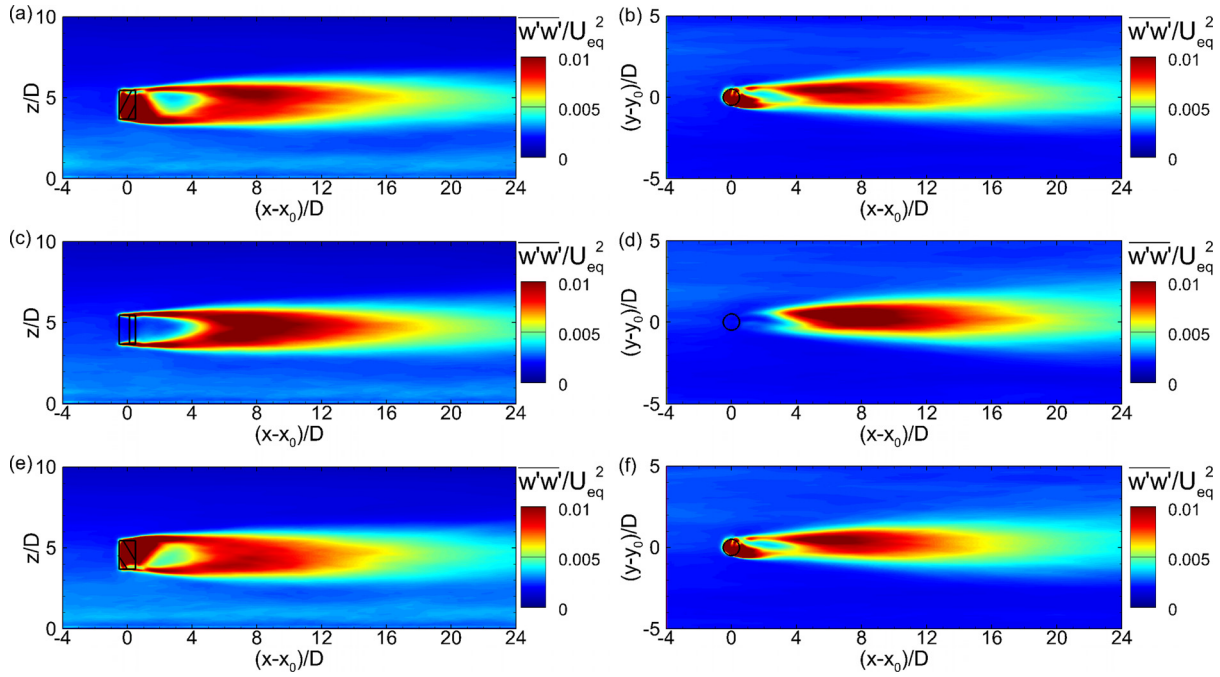

FIG. 20. Vertical velocity variance $\overline{w'w'}$ on the (x, z)-plane across the center axis of the VAWT (left column) and on the (x, y)-plane at the equator height (right column): (a) and (b) helical-bladed VAWT with $\gamma = -127^{\circ}$; (c) and (d) straight-bladed VAWT; (e) and (f) helical-bladed VAWT with $\gamma = 127^{\circ}$.

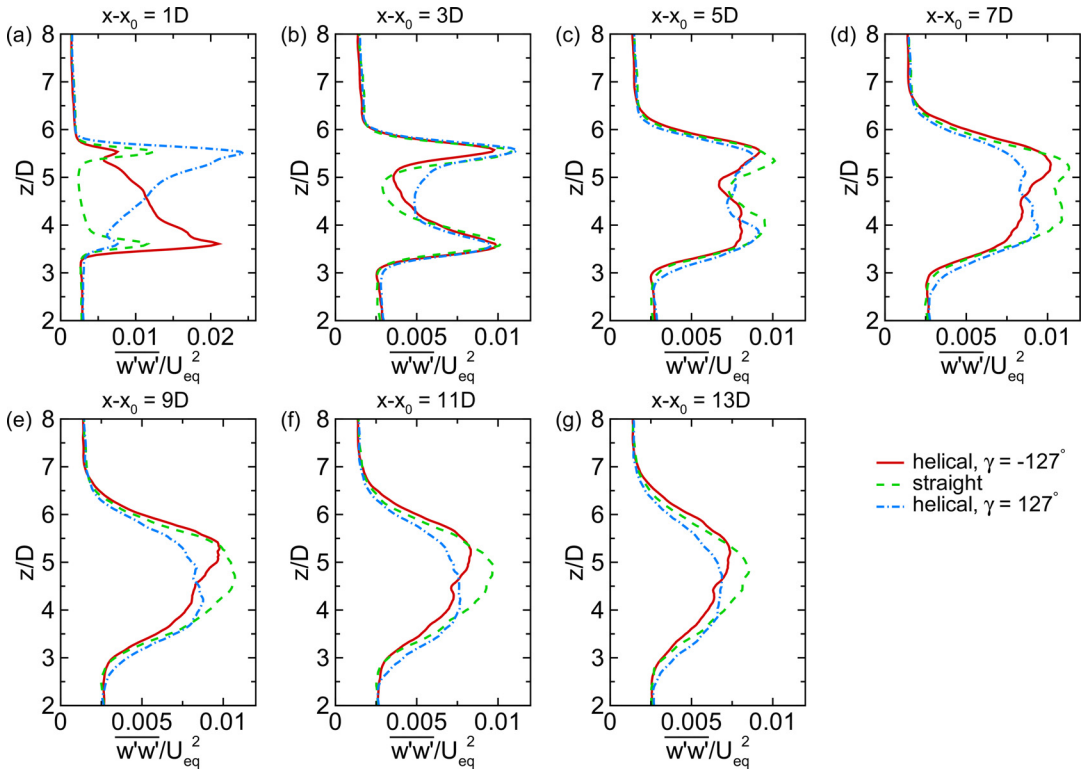

FIG. 21. Vertical profiles of $\overline{w'w'}$ along the wake centerline at different streamwise locations $(x - x_0) =$: (a) 1D; (b) 3D; (c) 5D; (d) 7D; (e) 9D; (f) 11D; and (g) 13D. Solid lines: helical-bladed VAWT with $\gamma = -127^{\circ}$; dashed lines: straight-bladed VAWT; dash-dot lines: helical-bladed VAWT with $\gamma = 127^{\circ}$.

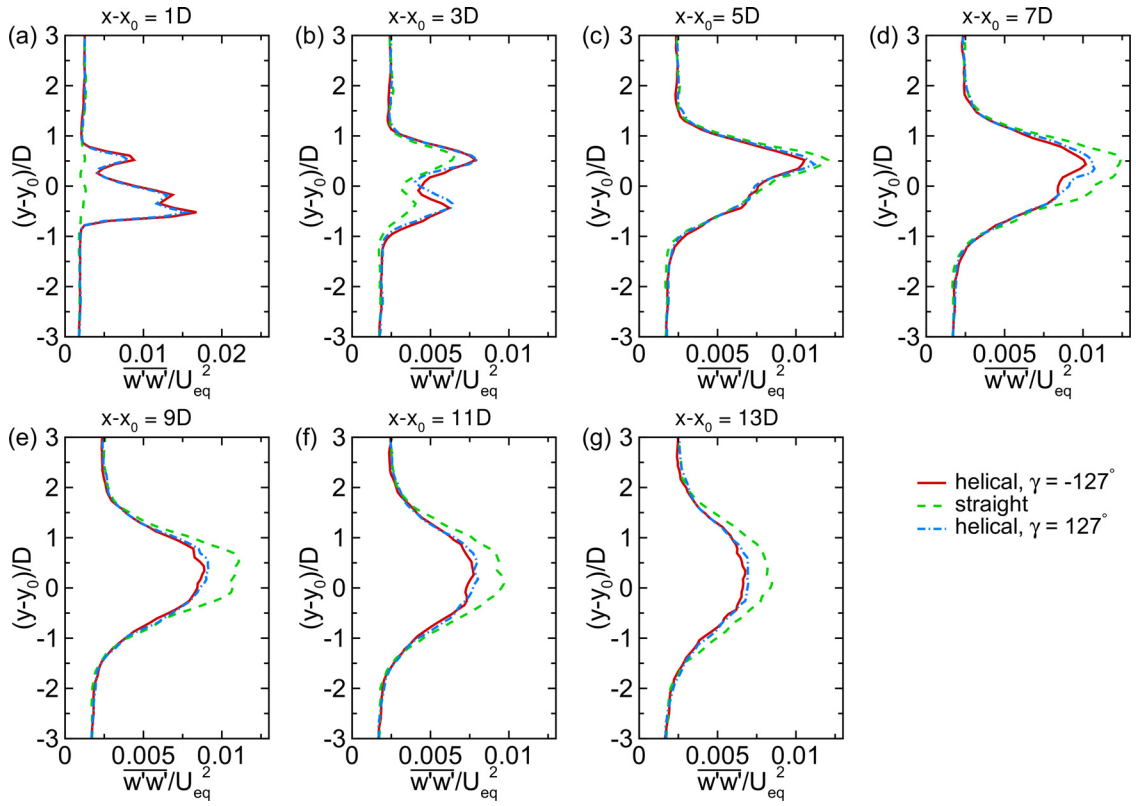

FIG. 22. Spanwise profiles of $\overline{w'w'}$ at the turbine equator height at different streamwise locations $(x - x_0) =$: (a) 1*D*; (b) 3*D*; (c) 5*D*; (d) 7*D*; (e) 9*D*; (f) 11*D*; and (g) 13*D*. Solid lines: helical-bladed VAWT with $\gamma = -127°$; dashed lines: straight-bladed VAWT; dash-dot lines: helical-bladed VAWT with $\gamma = 127°$.

vertical direction, respectively; $\overline{u'v'}$ and $\bar{\tau}_{yx}$ represent the resolved and unresolved (SGS) turbulent transport of streamwise momentum along the spanwise direction, respectively.

Figure 23 shows $\overline{u'w'}$ (left column) and $\bar{\tau}_{zx}$ (right column) on the (x, z)-plane across the center axis of the VAWT. Both $\overline{u'w'}$ and $\bar{\tau}_{zx}$ peak in the two shear layers at the upper and lower edges of the turbine wake region, with opposite signs (i.e., negative in the upper and positive in the lower layers, respectively) due to the reversed $\partial\bar{u}/\partial z$ in these two shear layers. The magnitude of $\bar{\tau}_{zx}$ is much smaller than that of $\overline{u'w'}$, indicating that the dynamically important turbulent flow effects have been well resolved in the current LES. Figure 24 shows the corresponding vertical profiles of $\overline{u'w'}$. The comparison between Figs. 23(a) and 23(c) shows that the magnitude of $\overline{u'w'}$ in the lower shear layer behind the helical-bladed VAWT with $\gamma = -127°$ is noticeably smaller than that in the case with straight-bladed VAWT. This effect can also been seen clearly in Figs. 24(c)–24(e). Conversely, reversing the blade twist angle to $\gamma = 127°$ causes the weakening of $\overline{u'w'}$ in the upper shear layer of the wake compared with that in the straight-bladed case [Figs. 23(e) and 24(c)–24(e)]. In the far-wake region at $x - x_0 \gtrsim 11D$, the difference in $\overline{u'w'}$ among the three cases becomes insignificant [Figs. 24(f) and 24(g)].

Figure 25 shows $\overline{u'v'}$ (left column) and $\bar{\tau}_{yx}$ (right column) on the (x, y)-plane at the turbine equator height, and Fig. 26 shows the corresponding spanwise profiles of $\overline{u'v'}$ at various streamwise locations. Both $\overline{u'v'}$ and $\bar{\tau}_{yx}$ peak in the two shear layers at the lateral edges of the turbine wake region, with opposite signs due to the reversed $\partial\bar{u}/\partial y$ in these two shear layers. Similar to $\bar{\tau}_{zx}$, the magnitude of $\bar{\tau}_{yx}$ is also much smaller than that of $\overline{u'v'}$. The effect of helical-shaped blades on $\overline{u'v'}$ is less significant than on $\overline{u'w'}$, suggesting the importance of the helical blade-induced vertical inclination on the wake turbulence characteristics.

F. VAWT wake visualization based on the transport-tube method

The mass-flux based stream tube[72,73] has been widely used as a useful tool for flow analysis and visualization. Meyers and Meneveau[74] further generalized this transport-tube concept and extended it to the visualization of momentum and energy transports. Here, this generalized transport tube method is applied to visualize the downstream development of the VAWT wakes.

The mean-flow stream tube can be easily constructed based on the time-averaged flow velocity vector field. For the kinetic energy transport tube, the steady-state transport equation for the mean-flow kinetic energy ($K = \bar{u}_i\bar{u}_i/2$) in the VAWT wake can be written in the index-notation form as[74]

$$\frac{\partial \bar{F}_{K,j}}{\partial x_j} = -\frac{1}{\rho}\frac{\partial(\bar{u}_i\bar{p})}{\partial x_i} + \overline{u_i'u_j'}\frac{\partial \bar{u}_i}{\partial x_j} + \bar{\tau}_{ij}\bar{S}_{ij}, \tag{20}$$

where

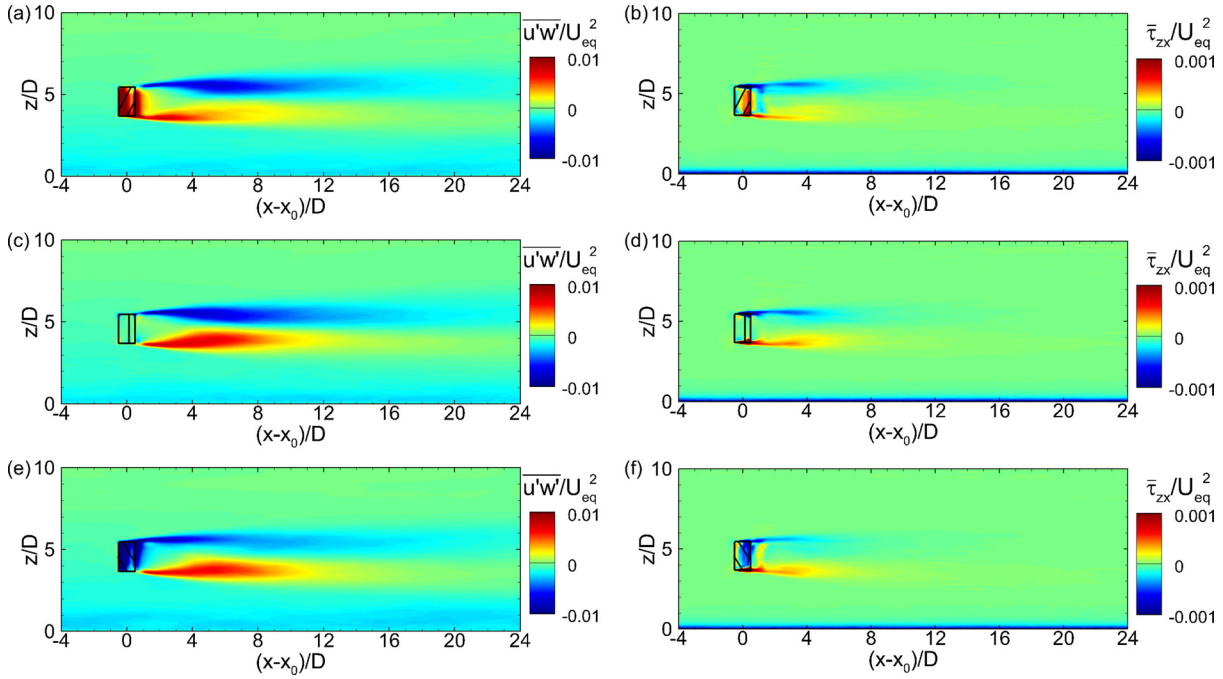

FIG. 23. Time-averaged Reynolds stress $\overline{u'w'}$ (left column) and SGS stress $\bar{\tau}_{zx}$ (right column) on the (x, z)-plane across the center axis of the VAWT: (a) and (b) helical-bladed VAWT with $\gamma = -127^{\circ}$; (c) and (d) straight-bladed VAWT; (e) and (f) helical-bladed VAWT with $\gamma = 127^{\circ}$.

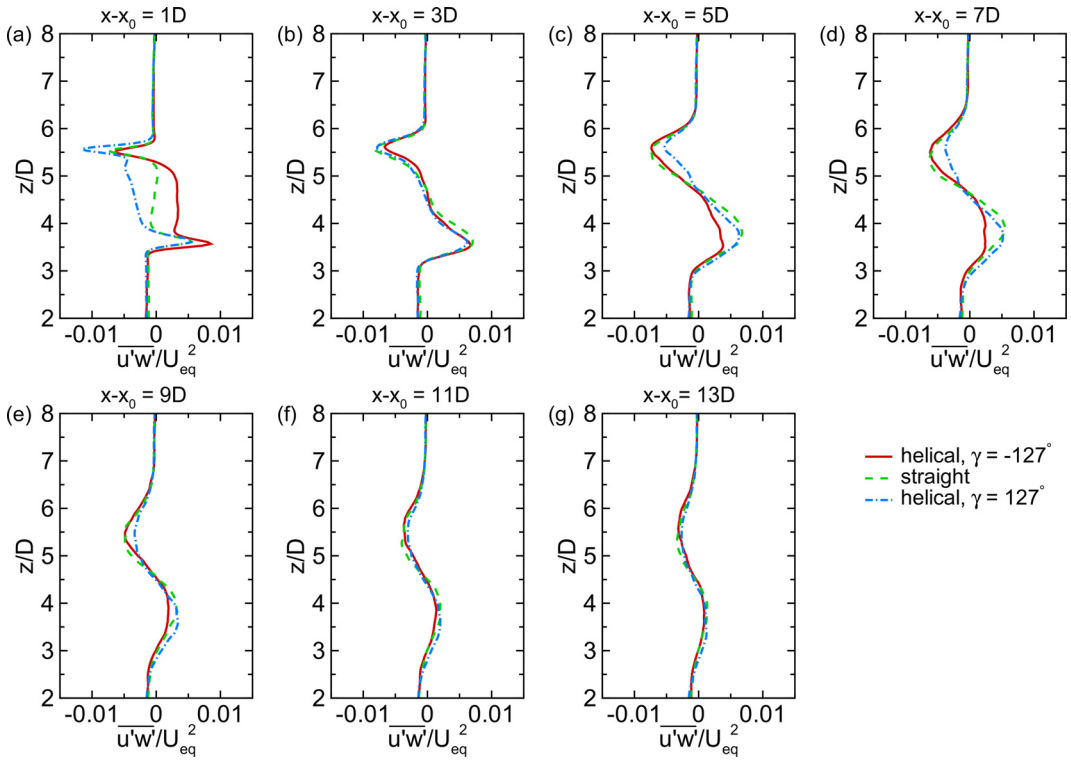

FIG. 24. Vertical profiles of $\overline{u'w'}$ along the wake centerline at different streamwise locations $(x - x_0) =$: (a) 1D; (b) 3D; (c) 5D; (d) 7D; (e) 9D; (f) 11D; and (g) 13D. Solid lines: helical-bladed VAWT with $\gamma = -127^{\circ}$; dashed lines: straight-bladed VAWT; dash-dot lines: helical-bladed VAWT with $\gamma = 127^{\circ}$.

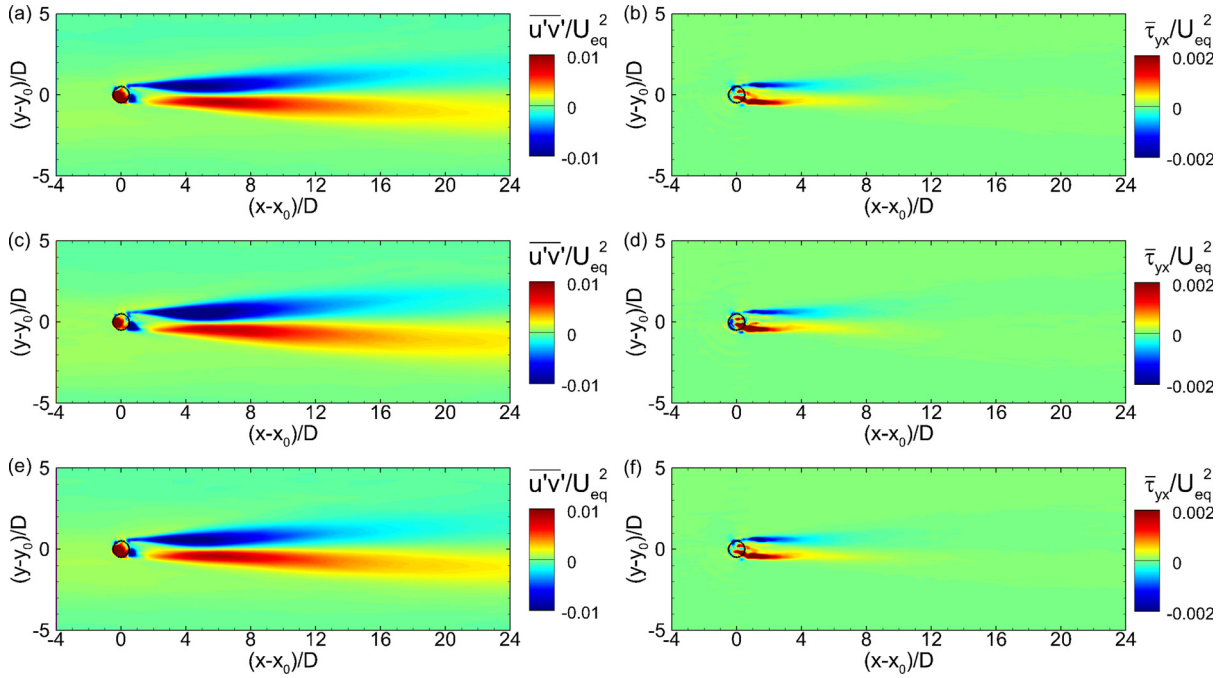

FIG. 25. Time-averaged Reynolds stress $\overline{u'v'}$ (left column) and SGS stress $\bar{\tau}_{yx}$ (right column) on the (x, y)-plane at the equator height of the VAWT: (a) and (b) helical-bladed VAWT with $\gamma = -127^{\circ}$; (c) and (d) straight-bladed VAWT; (e) and (f) helical-bladed VAWT with $\gamma = 127^{\circ}$.

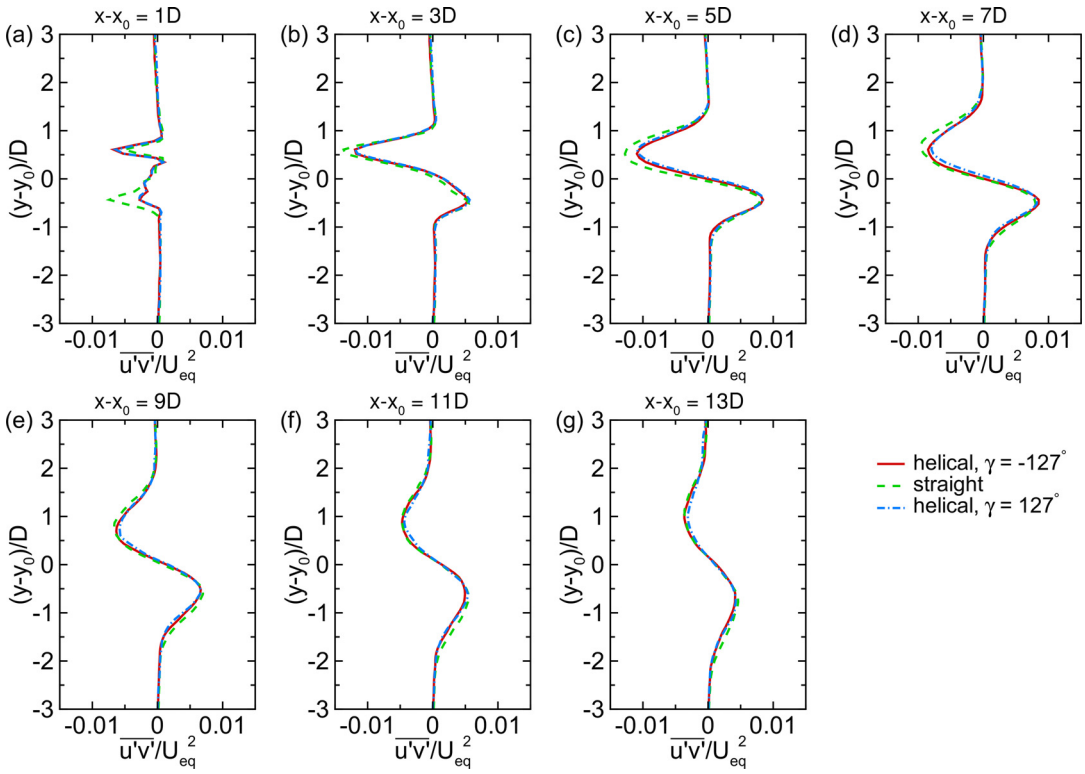

FIG. 26. Spanwise profiles of $\overline{u'v'}$ at the turbine equator height at different streamwise locations $(x - x_0) =$: (a) 1D; (b) 3D; (c) 5D; (d) 7D; (e) 9D; (f) 11D; and (g) 13D. Solid lines: helical-bladed VAWT with $\gamma = -127^{\circ}$; dashed lines: straight-bladed VAWT; dash-dot lines: helical-bladed VAWT with $\gamma = 127^{\circ}$.

$$\bar{F}_{K,j} = K\bar{u}_j + \overline{u_i'u_j'}\,\bar{u}_i + \bar{\tau}_{ij}\bar{u}_i \tag{21}$$

is the mean kinetic energy flux vector field per unit mass, $\bar{u}_i$ is the time-averaged velocity vector field, $u_i' = \tilde{u}_i - \bar{u}_i$ is the velocity fluctuation, $\tilde{u}_i$ is the LES-resolved instantaneous velocity as defined in Sec. II A, $\bar{\tau}_{ij}$ is the time-averaged SGS stress tensor, and $\bar{S}_{ij}$ is the time-averaged strain-rate tensor. The three terms on the right-hand side of Eq. (20) represent the pressure transport, mean-shear induced production, and SGS dissipation of the mean kinetic energy, respectively. Among these terms, the pressure transport is insignificant in the wake flow; the production $\overline{u_i'u_j'}(\partial\bar{u}_i/\partial x_j)$ acts as a sink term for K in Eq. (20), but appears as a source term (with a reversed sign) in the transport equation of the turbulent kinetic energy; and the SGS dissipation also acts as a sink term.

Based on $\bar{F}_{K,j}$, the corresponding kinetic energy transport velocity can be calculated as[74]

$$\bar{u}_{K,j} \equiv \bar{F}_{K,j}/K = \bar{u}_j + \overline{u_i'u_j'}\,\bar{u}_i/K + \bar{\tau}_{ij}\bar{u}_i/K, \tag{22}$$

where the three terms on the right-hand side of Eq. (22) represents the effects due to the mean-flow advection, the resolved turbulent transport, and the unresolved SGS transport. Recall that a stream tube for mass transport is defined as a tubular region of fluid surrounded by streamlines of mean velocity vector field $\bar{u}_j$. Analogous to the stream tube concept, a transport tube of mean kinetic energy is defined as a tubular region surrounded by the streamlines of the K-transport velocity $\bar{u}_{K,j}$. As shown in Figs. 23 and 25, the magnitudes of the SGS stress $\bar{\tau}_{ij}$ are much smaller than those of the corresponding Reynolds stress $\overline{u_i'u_j'}$. Thus, the difference between $\bar{u}_{K,j}$ and $\bar{u}_j$ is mainly due to the resolved turbulent transport as shown in Eq. (22).

Figure 27 shows the mean-flow stream tubes for the three VAWT cases. In each case, the stream tube is obtained by constructing streamlines from 120 seed points (evenly spaced based on the polar angle) on the (y, z)-plane at $x - x_0 = 1D$ along the elliptical circle

$$\left(\frac{y - y_0}{D/2}\right)^2 + \left(\frac{z - z_{eq}}{H/2}\right)^2 = 1. \tag{23}$$

For each VAWT case, the mass flow rate is conserved along the stream tube without mass fluxes through the tube mantle. At the starting cross-section of the stream tube at $x - x_0 = 1D$, the flow velocity within the tube is smaller than the free-stream velocity outside the VAWT wake. As the wake flow moves toward the downstream direction, the stream tube cross-section shrinks as the flow speed inside the tube recovers, and the free-stream fluid around the VAWT wake region flows inwards to fill the space. For the straight-bladed VAWT case, the stream tube exhibits considerable shrinkage both horizontally and vertically as it extends downstream, with the center of the tube

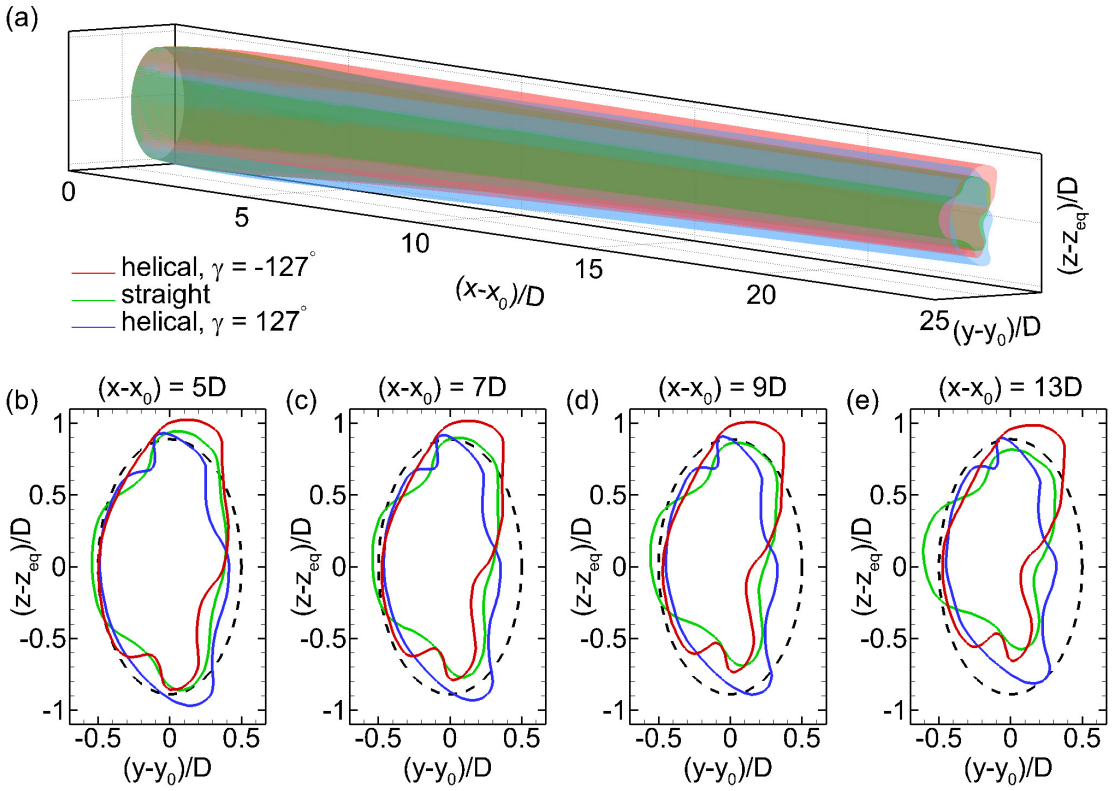

FIG. 27. Stream tubes in wake flows behind VAWTs. Panel (a) shows the three-dimensional view of the tubes: red for the helical-bladed VAWT with $\gamma = -127°$; green for the straight-bladed VAWT; blue for the helical-bladed VAWT with $\gamma = 127°$. Panels (b)–(e) show the (y, z)-plane views of the tube mantle at four different streamwise locations, in which the dashed line indicates the prescribed initial shape of the tube cross-section at $x - x_0 = 1D$, and the solid color lines correspond to the three VAWT cases shown in (a).

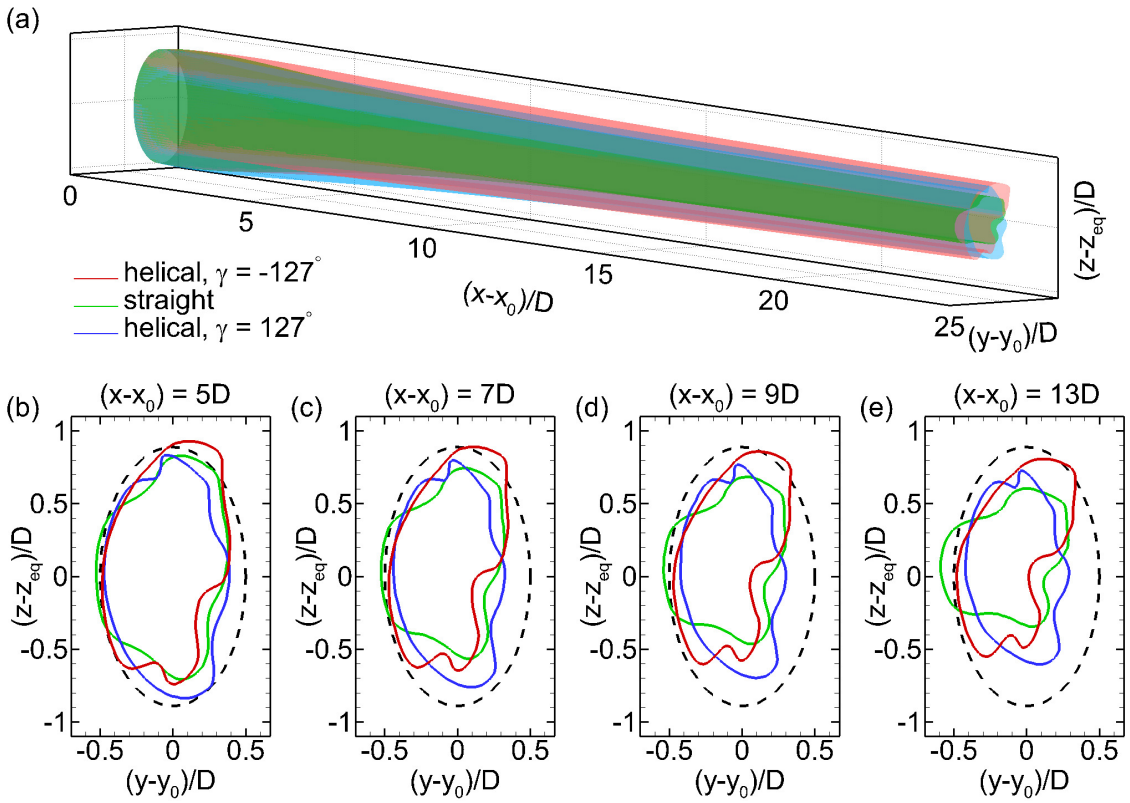

FIG. 28. Mean kinetic energy tubes in wake flows behind VAWTs. Panel (a) shows the three-dimensional view of the tubes: red for the helical-bladed VAWT with $\gamma = -127°$; green for the straight-bladed VAWT; blue for the helical-bladed VAWT with $\gamma = 127°$. Panels (b)–(e) show the (y, z)-plane views of the tube mantle at four different streamwise locations, in which the dashed line indicates the prescribed initial shape of the tube cross-section at $x - x_0 = 1D$, and the solid color lines correspond to the three VAWT cases shown in (a).

shifts toward $-y$ and $+z$ directions. By contrast, the stream tubes in the two helical-bladed VAWT cases exhibit less shrinkage in the vertical direction than that in the straight-bladed VAWT case. Moreover, the mean vertical velocity in the wake region induced by the helical blades (see Figs. 11 and 12) causes the center of the stream tube to be shifted upwards in the $\gamma = -127°$ case and downwards in the $\gamma = 127°$ case. Finally, the stream tube in the $\gamma = 127°$ case exhibits a leftward tilt with respect to the vertical that increases with downstream distance, while the stream tube in the $\gamma = -127°$ case shows an increasing rightward tilt. These behaviors were also observed in the field experiments of Wei *et al.*,[22] further suggesting that the LES models in the present study are representative of the flow phenomena around full-scale VAWTs in field conditions.

Figure 28 shows the mean-flow kinetic energy transport tubes constructed in a similar way as the stream tubes shown in Fig. 27 but based on the K-transport velocity $\bar{u}_{K,j}$ defined in Eq. (22). Similar to the stream tubes, the kinetic energy transport tubes also exhibit shrinkage as they extend downstream. Due to the additional effect of the resolved turbulent mixing, i.e., the second term in Eq. (22), the shrinkage of the mean kinetic transport tube is much more significant than that of the corresponding stream tube. Unlike the stream tube in which the mass flow rate is conserved, the mean kinetic energy is not conserved in the wake flow along the K transport tube due to the two sink terms in Eq. (20). Nevertheless, the transport tubes visualized in Fig. 28 still possess an important property similar to the stream tube, i.e., no flux of mean kinetic energy across the tube mantles.[74] Taking Fig. 28(e) as an example, the difference between a specific local tube mantle at $x - x_0 = 13D$ and the reference elliptical initial tube shape at $x - x_0 = 1D$ provides direct visualization of how the mean kinetic energy gets entrained from the high-speed surrounding flow into the wake region to help the recovery of the wind speed. For example, the red line shown in Fig. 28(e) indicates that for the helical-bladed VAWT with $\gamma = -127°$, the kinetic energy for recovering the mean wake flow speed is mainly from the free-stream flow on the $+y$ and $-z$ sides of the wake region. Overall, the stream tubes and kinetic energy transport tubes visualized in Figs. 27 and 28 show noticeable differences among the three VAWT cases, indicating that the blade geometry of the VAWT can induce considerable effects on the mass and energy transport in the turbine wake region.

V. CONCLUSIONS AND DISCUSSIONS

In the current work, we analyze the effect of helical blade geometry on the characteristics of VAWT wake flows based on simulation data obtained from the LES. The Johns Hopkins LESGO model is adopted to simulate the boundary layer turbulence, in which the effect of the VAWT on the wind is modeled using the ALM. Using this LES

model, the turbulent wake flows behind two representative helical-bladed VAWTs with opposite blade twist angles ($\gamma = \pm 127^\circ$) are simulated and analyzed. One additional case based on a straight-bladed VAWT with identical key parameters as the helical-bladed VAWTs is also simulated and used as a reference case.

The effects of the helical-shaped blades on the VAWT wake flow can be observed from the instantaneous flow fields, the time-averaged statistics of the mean flow velocities, and the turbulent statistics. In particular, the twisted blades of the helical VAWTs are found to enhance the streamwise and vertical velocity fluctuations in the near-wake region of the turbines. The rotating helical blades also generate a secondary vertical flow motion in the wake region, which is found to affect the characteristics of the turbulent wake flow. Taking the $\gamma = -127^\circ$ case as an example, the rotating helical blades push the flow downwards, resulting in the mean downward flow motions at $y - y_0 \approx \pm 0.5D$ and the upward counter flow at $-0.5D < y - y_0 < 0.5D$ in the turbine wake that extends to $x - x_0 \approx 10D$ (Figs. 11 and 12). This means that the vertical flow inclines the turbine wake upwards and weakens the shear $\partial\bar{u}/\partial z$. Consequently, the turbulent fluctuations $\overline{u'u'}$, $\overline{w'w'}$, and $\overline{u'w'}$ are also weakened in the lower shear layer near the bottom of the turbine wake region. The simulation and statistical analysis results of the $\gamma = 127^\circ$ case show that reversing the twist direction of the helical blades cause the aforementioned effects of the helical-bladed VAWT on the wake characteristics to be reversed. The wake-flow visualizations based on the transport-tube method also show considerable differences among the three VAWT cases regarding the transport of mass and kinetic energy from the surrounding free-stream flow into the turbine wake region.

To date, the characteristics of turbulent wake flows behind helical-bladed VAWTs have not been well understood compared to those for the straight-bladed VAWTs. As a result, there exist many different designs for helical-bladed VAWTs. More systematic studies are needed to help converge different design strategies into an optimal solution. Due to the high computational cost associated with the concurrent precursor simulation and the domain size for capturing the correct flow physics of the boundary layer turbulence, in the present study only a limited number of cases are studied. Nevertheless, this work still identifies potential mechanisms that can affect momentum transfer, wake recovery, and wake topology. These insights can inform the design of VAWT farms, and the apparent dependence of these trends on blade twist angle can be leveraged to further optimize energy transfer in helical-bladed VAWT arrays. For example, a VAWT with a positive twist angle (e.g., the $\gamma = 127^\circ$ VAWT studied in this work) can induce a downward inclination of the turbine wake and result in a noticeable reduction of the turbulent fluctuations [see, e.g., Figs. 18(c)–18(e) and 21(c)–21(e)] in the inflow of a downstream VAWT. This reduction of turbulent intensity is also more significant toward the upper end of the VAWT rotor height. As a result, the turbulence-induced fluctuations in the aerodynamic forces on the blades and the bending moment on the root of the rotor shaft may be significantly reduced, which can increase the longevity of the VAWTs used in a large wind farm.

ACKNOWLEDGMENTS

This research was supported by the National Science Foundation Fluid Dynamics Program under Grant No. 1804214 to D.Y. and Grant Nos. 1802476 and 2038071 to J.O.D. N.J.W. acknowledges support from the National Science Foundation Graduate Research Fellowship. M.G. and D.Y. acknowledge the use of the Sabine and Carya clusters from the Research Computing Data Core (RCDC) at the University of Houston to carry out the numerical simulations and data analyses presented in this manuscript. M.G. and D.Y. also thanks Vincent V. S. Laroche for his contribution to the initial development of the Transport Tube visualization tool. This work was authored in part by the National Renewable Energy Laboratory, operated by Alliance for Sustainable Energy, LLC, for the U.S. Department of Energy (DOE) under Contract No. DE-AC36-08GO28308. Funding provided by the U.S. Department of Energy Office of Energy Efficiency and Renewable Energy Wind Energy Technologies Office. The views expressed in the article do not necessarily represent the views of the DOE or the U.S. Government. The U.S. Government retains and the publisher, by accepting the article for publication, acknowledges that the U.S. Government retains a nonexclusive, paid-up, irrevocable, worldwide license to publish or reproduce the published form of this work, or allow others to do so, for U.S. Government purposes.

AUTHOR DECLARATIONS

Conflict of Interest

The authors have no conflicts to disclose.

Author Contributions

Masoumeh Gharaati: Conceptualization (equal); Data curation (lead); Formal analysis (lead); Investigation (equal); Methodology (equal); Validation (lead); Visualization (lead); Writing – original draft (equal); Writing – review and editing (equal). **Shuolin Xiao:** Investigation (supporting); Methodology (equal); Software (equal); Writing – review and editing (equal). **Nathaniel J. Wei:** Conceptualization (supporting); Investigation (supporting); Writing – review and editing (equal). **Luis A Martinez-Tossas:** Investigation (supporting); Methodology (supporting); Software (equal); Writing – review and editing (equal). **John O. Dabiri:** Conceptualization (supporting); Funding acquisition (equal); Investigation (supporting); Project administration (supporting); Supervision (equal); Writing – review and editing (equal). **Di Yang:** Conceptualization (lead); Funding acquisition (equal); Investigation (lead); Methodology (lead); Project administration (lead); Resources (lead); Supervision (lead); Writing – original draft (lead).

DATA AVAILABILITY

The data that support the findings of this study are available from the corresponding author upon reasonable request.

REFERENCES

[1]J. F. Manwell, J. G. McGowan, and A. L. Rogers, *Wind Energy Explained*, 2nd ed. (Wiley, 2009).
[2]T. Burton, N. Jenkins, D. Sharpe, and E. Bossanyi, *Wind Energy Handbook* (Wiley, 2011).
[3]W. Short and N. Blair, "20% Wind energy by 2030: Increasing wind energy's contribution to US electricity supply," Technical Report No. DOE/GO-102008-2567 (U.S. Department of Energy, 2008).
[4]P. Jain, *Wind Energy Engineering*, 2nd ed. (McGraw Hill, 2016).
[5]T. Letcher, *Wind Energy Engineering: A Handbook for Onshore and Offshore Wind Turbines*, 1st ed. (Academic Press, 2017).

[6]F. Porté-Agel, M. Bastankhah, and S. Shamsoddin, "Wind-turbine and wind-farm flows: A review," Boundary-Layer Meteorol. **174**, 1–59 (2020).
[7]J. Meyers and C. Meneveau, "Optimal turbine spacing in fully developed wind farm boundary layers," Wind Energy **15**, 305–317 (2012).
[8]J. Contrell, T. Stehly, J. Johnson, J. O. Roberts, Z. Parker, G. Scott, and D. Heimiller, "Analysis of transportation and logistics challenges affecting the deployment of larger wind turbines: Summary of results," Technical Report No. NREL/TP-5000-61063 (National Renewable Energy Laboratory, 2014).
[9]J. Yang, L. Fang, D. Song, M. Su, X. Yang, L. Huang, and Y. H. Joo, "Review of control strategy of large horizontal-axis wind turbines yaw system," Wind Energy **24**, 97–115 (2021).
[10]M. Kinzel, Q. Mulligan, and J. O. Dabiri, "Energy exchange in an array of vertical-axis wind turbines," J. Turbul. **13**, N38 (2012).
[11]J. O. Dabiri, "Potential order-of-magnitude enhancement of wind farm power density via counter-rotating vertical-axis wind turbine arrays," J. Renewable Sustainable Energy **3**, 043104 (2011).
[12]I. D. Brownstein, N. J. Wei, and J. O. Dabiri, "Aerodynamically interacting vertical-axis wind turbines: Performance enhancement and three-dimensional flow," Energies **12**, 2724 (2019).
[13]M. Casini, "Small vertical axis wind turbines for energy efficiency of buildings," J. Clean Energy Technol. **4**, 56–65 (2016).
[14]S. H. Hezaveh, E. Bou-Zeid, M. W. Lohry, and L. Martinelli, "Simulation and wake analysis of a single vertical axis wind turbine," Wind Energy **20**, 713–730 (2017).
[15]G. Brochier, P. Fraunie, C. Beguier, and I. Paraschivoiu, "Water channel experiments of dynamic stall on Darrieus wind turbine blades," J. Propul. Power **2**, 445–449 (1986).
[16]P. Bachant and M. Wosnik, "Performance and near-wake measurements for a vertical axis turbine at moderate Reynolds number," in Proceedings of the ASME Fluids Engineering Summer Meeting (2013).
[17]D. B. Araya and J. O. Dabiri, "A comparison of wake measurements in motor-driven and flow-driven turbine experiments," Exp. Fluids **56**, 150 (2015).
[18]M. Kinzel, D. B. Araya, and J. O. Dabiri, "Turbulence in vertical axis wind turbine canopies," Phys. Fluids **27**, 115102 (2015).
[19]D. B. Araya and J. O. Dabiri, "Vertical axis wind turbine in a falling soap film," Phys. Fluids **27**, 091108 (2015).
[20]D. B. Araya, T. Colonius, and J. O. Dabiri, "Transition to bluff-body dynamics in the wake of vertical-axis wind turbines," J. Fluid Mech. **813**, 346–381 (2017).
[21]S. H. Hezaveh, E. Bou-Zeid, G. Cortina, L. Martinelli, J. Dabiri, and M. Kinzel, "Increasing the power production of vertical-axis wind-turbine farms using synergistic clustering," Boundary-Layer Meteorol. **169**, 275–296 (2018).
[22]N. J. Wei, I. D. Brownstein, J. L. Cardona, M. F. Howland, and J. O. Dabiri, "Near-wake structure of full-scale vertical-axis wind turbines," J. Fluid Mech. **914**, A17 (2021).
[23]K. J. Ryan, F. Coletti, C. J. Elkins, J. O. Dabiri, and J. K. Eaton, "Three-dimensional flow field around and downstream of a subscale model rotating vertical axis wind turbine," Exp. Fluids **57**, 38 (2016).
[24]C. Pearson, "Vertical axis wind turbine acoustics," Ph.D. thesis (Cambridge University, 2013).
[25]A. Alaimo, A. Esposito, A. Messineo, C. Orlando, and D. Tumino, "3D CFD analysis of a vertical axis wind turbine," Energies **8**, 3013–3033 (2015).
[26]M. Moghimi and H. Motawej, "Developed DMST model for performance analysis and parametric evaluation of Gorlov vertical axis wind turbines," Sustainable Energy Technol. Assess. **37**, 100616 (2020).
[27]Q. Cheng, X. Liu, H. S. Ji, K. C. Kim, and B. Yang, "Aerodynamic analysis of a helical vertical axis wind turbine," Energies **10**, 575 (2017).
[28]U. Divakaran, A. Ramesh, A. Mohammad, and R. K. Velamati, "Effect of helix angle on the performance of helical vertical axis wind turbine," Energies **14**, 393 (2021).
[29]R. B. Cal, J. Lebrón, L. Castillo, H. S. Kang, and C. Meneveau, "Experimental study of the horizontally averaged flow structure in a model wind-turbine array boundary layer," J. Renewable Sustainable Energy **2**, 013106 (2010).
[30]M. Calaf, C. Meneveau, and J. Meyers, "Large eddy simulation study of fully developed wind-turbine array boundary layers," Phys. Fluids **22**, 015110 (2010).
[31]N. Hamilton, H. S. Kang, C. Meneveau, and R. Bayoán Cal, "Statistical analysis of kinetic energy entrainment in a model wind turbine array boundary layer," J. Renewable Sustainable Energy **4**, 063105 (2012).
[32]J. Bremseth and K. Duraisamy, "Computational analysis of vertical axis wind turbine arrays," Theor. Comput. Fluid Dyn. **30**, 387–401 (2016).
[33]S. Xie, C. L. Archer, N. Ghaisas, and C. Meneveau, "Benefits of collocating vertical-axis and horizontal-axis wind turbines in large wind farms," Wind Energy **20**, 45–62 (2017).
[34]S. El-Asha, L. Zhan, and G. V. Iungo, "Quantification of power losses due to wind turbine wake interactions through SCADA, meteorological and wind LiDAR data," Wind Energy **20**, 1823–1839 (2017).
[35]M. Calaf, M. B. Parlange, and C. Meneveau, "Large eddy simulation study of scalar transport in fully developed wind-turbine array boundary layers," Phys. Fluids **23**, 126603 (2011).
[36]D. Yang, C. Meneveau, and L. Shen, "Large-eddy simulation of offshore wind farm," Phys. Fluids **26**, 025101 (2014).
[37]L. A. Martínez Tossas, R. J. Stevens, and C. Meneveau, "Wind farm large-eddy simulations on very coarse grid resolutions using an actuator line model," AIAA Paper No. 2016-1261, 2016.
[38]S. Shamsoddin and F. Porté-Agel, "A large-eddy simulation study of vertical axis wind turbine wakes in the atmospheric boundary layer," Energies **9**, 366 (2016).
[39]J. N. Sørensen and W. Z. Shen, "Numerical modeling of wind turbine wakes," J. Fluids Eng. **124**, 393–399 (2002).
[40]S. Shamsoddin and F. Porté-Agel, "Large eddy simulation of vertical axis wind turbine wakes," Energies **7**, 890–912 (2014).
[41]L. A. Martínez-Tossas, M. J. Churchfield, and S. Leonardi, "Large eddy simulations of the flow past wind turbines: Actuator line and disk modeling," Wind Energy **18**, 1047–1060 (2015).
[42]L. A. Martínez-Tossas, M. J. Churchfield, and C. Meneveau, "A highly resolved large-eddy simulation of a wind turbine using an actuator line model with optimal body force projection," J. Phys. **753**, 082014 (2016).
[43]H. Sarlak, T. Nishino, L. A. Martínez-Tossas, C. Meneveau, and J. N. Sørensen, "Assessment of blockage effects on the wake characteristics and power of wind turbines," Renewable Energy **93**, 340–352 (2016).
[44]M. Abkar and J. O. Dabiri, "Self-similarity and flow characteristics of vertical-axis wind turbine wakes: An LES study," J. Turbul. **18**, 373–389 (2017).
[45]M. J. Churchfield, S. Schreck, L. A. Martínez-Tossas, C. Meneveau, and P. R. Spalart, "An advanced actuator line method for wind energy applications and beyond," AIAA Paper No. 2017-1998, 2017.
[46]V. Mendoza and A. Goude, "Wake flow simulation of a vertical axis wind turbine under the influence of wind shear," J. Phys. **854**, 012031 (2017).
[47]V. Mendoza, P. Bachant, C. Ferreira, and A. Goude, "Near-wake flow simulation of a vertical axis turbine using an actuator line model," Wind Energy **22**, 171–188 (2019).
[48]V. Mendoza, A. Chaudhari, and A. Goude, "Performance and wake comparison of horizontal and vertical axis wind turbines under varying surface roughness conditions," Wind Energy **22**, 458–472 (2019).
[49]See https://lesgo.me.jhu.edu/ for "LESGO: A Parallel Pseudo-Spectral Large-Eddy Simulation Code."
[50]L. A. Martínez-Tossas, M. J. Churchfield, A. E. Yilmaz, H. Sarlak, P. L. Johnson, J. N. Sørensen, J. Meyers, and C. Meneveau, "Comparison of four large-eddy simulation research codes and effects of model coefficient and inflow turbulence in actuator-line-based wind turbine modeling," J. Renewable Sustainable Energy **10**, 033301 (2018).
[51]J. Smagorinsky, "General circulation experiments with the primitive equations," Mon. Weather Rev. **91**, 99–164 (1963).
[52]D. K. Lilly, "The representation of small-scale turbulence in numerical simulation experiments," in Proceedings of the IBM Scientific Computing Symposium on Environmental Sciences (1967).
[53]C.-H. Moeng, "A large-eddy-simulation model for the study of planetary boundary-layer turbulence," J. Atmos. Sci. **41**, 2052–2062 (1984).
[54]M. Germano, U. Piomelli, P. Moin, and W. H. Cabot, "A dynamic subgrid-scale eddy viscosity model," Phys. Fluids **3**, 1760–1765 (1991).
[55]S. P. Pope, *Turbulent Flows* (Cambridge University Press, 2000).
[56]E. Bou-Zeid, C. Meneveau, and M. Parlange, "A scale-dependent Lagrangian dynamic model for large eddy simulation of complex turbulent flows," Phys. Fluids **17**, 025105 (2005).

[57]Y. Wu and F. Porté-Agel, "Large-eddy simulation of wind-turbine wakes: Evaluation of turbine parametrisations," Boundary-Layer Meteorol. **138**, 345–366 (2011).
[58]D. Yang, C. Meneveau, and L. Shen, "Effect of downwind swells on offshore wind energy harvesting: A large-eddy simulation study," Renewable Energy **70**, 11–23 (2014).
[59]S. Xiao and D. Yang, "Large-eddy simulation-based study of effect of swell-induced pitch motion on wake-flow statistics and power extraction of offshore wind turbines," Energies **12**, 1246 (2019).
[60]R. J. Stevens, J. Graham, and C. Meneveau, "A concurrent precursor inflow method for large eddy simulations and applications to finite length wind farms," Renewable Energy **68**, 46–50 (2014).
[61]P. Schlatter, N. Adams, and L. Kleiser, "A windowing method for periodic inflow/outflow boundary treatment of non-periodic flows," J. Comput. Phys. **206**, 505–535 (2005).
[62]S. Chester, C. Meneveau, and M. B. Parlange, "Modeling turbulent flow over fractal trees with renormalized numerical simulation," J. Comput. Phys. **225**, 427–448 (2007).
[63]W. J. McCroskey, "The phenomenon of dynamic stall," Technical Report No. 81264 (NASA, 1981).
[64]R. Gormont, "A mathematical model of unsteady aerodynamics and radial flow for application to helicopter rotors," Technical Report No. 72-67 (Army Air Mobility Research and Development Laboratory, 1973).
[65]R. E. Sheldahl and P. C. Klimas, "Aerodynamic characteristics of seven symmetrical airfoil sections through 180-degree angle of attack for use in aerodynamic analysis of vertical axis wind turbines," Technical Report No. SAND-80-2114 (Sandia National Labs, 1981).
[66]P. Bachant and M. Wosnik, "Characterising the near-wake of a cross-flow turbine," J. Turbul. **16**, 392–410 (2015).
[67]S. A. Orszag and Y.-H. Pao, "Numerical computation of turbulent shear flows," Adv. Geophys. **18A**, 225–236 (1975).
[68]J. H. Ferziger and M. Perić, *Computational Methods for Fluid Dynamics*, 1st ed. (Springer, 1996).
[69]J. Albertson and M. Parlange, "Surface length scales and shear stress: Implications for land-atmosphere interaction over complex terrain," Water Resour. Res. **35**, 2121–2132, https://doi.org/10.1029/1999WR900094 (1999).
[70]S. A. Orszag, "Transform method for the calculation of vector-coupled sums: Application to the spectral form of the vorticity equation," J. Atmos. Sci. **27**, 890–894 (1970).
[71]J. D. Albertson, "Large eddy simulation of land-atmosphere interaction," Ph.D. thesis (University of California, Davis, 1996).
[72]G. K. Batchelor, *An Introduction to Fluid Dynamics* (Cambridge University Press, 1967).
[73]J. Fay, *Introduction to Fluid Mechanics* (MIT Press, 1994).
[74]J. Meyers and C. Meneveau, "Flow visualization using momentum and energy transport tubes and applications to turbulent flow in wind farms," J. Fluid Mech. **715**, 335–358 (2013).